Mobile Power Plants; Waste Body Heat Recovery

by

Jonathan S. Gibbons

and

Stephen V. Samouhos

Submitted to the Department of Mechanical
Engineering in Partial Fulfillment
of the Requirements for the Degree of

Bachelor of Science

at the

Massachusetts Institute of Technology

June 2004

Signatures of Authors.....

Department of Mechanical Engineering
May 7, 2004

Certified by.....

Todd A. Thorsen
Assistant Professor of Mechanical Engineering
Thesis Supervisor

Accepted by.....

Ernest G. Cravalho
Chairman, Undergraduate Thesis Committee
Professor of Mechanical Engineering

Mobile Power Plants; Waste Body Heat Recovery

by

Jonathan S. Gibbons

and

Stephen V. Samouhos

Submitted to the Department of Mechanical Engineering
on June 7, 2004 in Partial Fulfillment of the
Requirements for the Degree of Bachelor of Science in
Mechanical Engineering

ABSTRACT

Novel methods to convert waste metabolic heat into useful and useable amounts of electricity were studied. Thermoelectric, magneto hydrodynamic, and piezo-electric energy conversions at the desired scope were evaluated to understand their role and utility in the efficient conversion of waste body heat. The piezo-electric generator holds the most promise for the efficient conversion of waste body heat into electricity. In the future, this same device could be easily extended into a combustion based power plant.

An experimental apparatus investigating the use of magneto hydrodynamics was designed, built, and tested. A room temperature liquid metal was propelled through a magneto hydrodynamic channel of 4 inches by 0.1875 inches at a rate of 10 mL/s. A 2 T induction field was applied within the channel. However, the results of the analysis did not find the magneto hydrodynamic device to be an effective electric generator at the scale tested.

Thesis Supervisor: Todd A. Thorsen

Title: Assistant Professor of Mechanical Engineering

To my parents,
For everything they've done
To get me this far

—Jonathan S. Gibbons

To my loving parents,
The team that is always there.
To the spirit that drives,
Thank you.

—Stephen V. Samouhos

Chapter 1: The Energy Crisis

Mobile power is a critical issue for the development of our mobile electronics capabilities. Consumers depend on the battery in their cell phones and lap tops for everyday activities. The effects of power loss in any mobile communication or data processing unit can be devastating. In certain cases power loss can even be fatal; the survival of the dismounted foot soldier for instance, depends on the status of his mobile electronics.

The near future electrical energy needs of the dismounted soldier exceed the utility of current commercial batteries.[1] Even now, the limitations of batteries ultimately prevent the soldier from using more advanced weapons, communications and defense systems that are critical for mission success and soldier survival.[2]

	Functional Operating Power (W)
Computer/Radio Subsystem	
Computer	14.800
Hand-Held Flat Panel Display	6.400
Soldier Radio	
Receive	1.400
Transmit	6.000
Squad Radio	
Receive	2.000
Transmit	12.000
Global Positioning System	1.500
Video Capture	1.000
Subtotal	45.100
Integrated Helmet and Sight Subsystem (IHAS)	
Laser Detectors	0.600
Helmet-Mounted Display	4.900
Imager	0.100
Subtotal	5.600
Weapon Subsystem	
Laser Rangefinder	0.050
Laser Aiming Light	0.075
Digital Compass	0.350
Thermal Weapon Sight	5.525
Subtotal	6.000
TOTAL	56.7

Figure 1.1. Land Warrior system power requirements with 1997 electronic devices. Land Warrior system deployment is expected by 2005 (EET report p. 66)

The army seeks to solve this problem via mobile power generators, of which the palm power and fuel cell programs are the most notable.[3] Using current electronics, the future soldier systems require an enormous amount of power. The electronics industry is also fighting the power battle by reducing the electricity consumption of devices.

Computer

2001 (0.15 W) 150 MIPS computation requirement required for I/O functions, such as speech recognition at 1 mW/MIPS.

2015 (0.01 W) 1,000 MIPS computation requirement at 10 μW/MIPS

Hand-Held Flat Panel Display

2001 (0.2 W) Reflective LCD displays commercially available for "personal digital assistants" require 0.2 W for a monochromatic (640 x 480) display.

2015 (0.007 W) Display technologies allowing refresh rates of 1 frame/sec will reduce power by a factor of 30.

Soldier Radio (receive)

2001 (0.1 W) Includes 30 MIPS of programmable DSP at 1 mW/MIPS, 200 MIPS of dedicated DSP (0.1 mW/MIPS) for security and advanced radio functions, and 50 mW of analog processing such as the power used for commercial cellular radios (e.g., GSM).

2015 (0.025 W) Analog processing will be a factor of two lower than the 2001 requirement and the digital processing will be reduced by a factor of 100 (becoming negligible).

Soldier Radio (transmit)

2001 (1.6 W) Power for the transmit amplifier will require 1.5 W, with the remainder of the functions similar to the 0.1 W requirement for receive functions above.

2015 (1.52 W) Power for the transmit amplifier will still require 1.5 W, with the remainder reduced to 0.025 mW.

Figure 1.2. Expected decreases in power consumption for critical electronics, and reasons for alteration. (EET report, p.72)

Other key devices such as the laser range finder and infrared night vision are also expected to have marked decreases in power consumption within the next 5 years. The current foot soldier carries a pair of night vision goggles, laser range finder, GPS, small radio, and flashlight. To power these devices, the dismounted rifleman carries a dozen

AA batteries for a 72 hour mission.[4] Missions often run longer and soldiers are forced to refill their battery suite in order to maintain their effectiveness in the field.

With current battery energy densities, this battery load provides 360 kJ, at a daily time averaged rate of 1.4 W. A dozen batteries supply enough power for 6 hours of night vision, 50+ hours of laser sight, and intermittent use of the rest of the soldier's electronic arsenal. At 5 W, the night vision device requires the greatest power. The land warrior system, which is scheduled for fielding by 2015, will require a significant increase in mobile power. By that time, however, it is expected that mobile power plants such as the palm power and fuel cell will be ready for deployment with soldiers.[5] Until 2015 and the implementation of advanced power systems, however, the dismounted soldier will still suffer from a lack of electrical power. Moreover, the effects of batteries extend beyond power limitation; a recent article published by Reuters explained how Iraqi soldiers tracked US army movements by following trails of dead batteries left in the sand.[6]

Our product strategy is for the short term solution of the soldier energy problem. We wish to produce a fielded 5W power system within one year. Such a bold target requires a simple, affordable and easily manufactured mobile power system. Furthermore, the device must adhere to strict restrictions; additional pounds, sensible thermal or acoustic signatures, unwieldy shapes and flimsy construction are not acceptable.

The energy conversion principles outlined in this document offer simple alternatives to satisfy all of these power constraints. To begin with, fuel or battery weight is mitigated by harnessing waste body heat for electricity production. Our analysis indicates that this is a viable alternative to batteries, provided that an efficient conversion

scheme is employed. Several unique benefits of waste body heat recovery are explored in the ensuing power plant schemes. Additionally, chapter five, which details piezoelectric MEMS devices, will also contain design criteria for an octane combustion based power plant.

The power and energy demands of mobile electronics are a critical component of our energy strategy. The rifleman's mobile electronics function in the 100 mW to 5W range. This meso-scale power range is a niche that remains unclaimed by generation devices. As devices operate on less power the importance of this niche will become ever more apparent. Figure 1.2 indicates that devices in the very near future will consume far less power. Hence, a simple, reliable system that produces 3W would satisfy the majority of future commercial mobile power needs. The product designed here is tailored to the military but could easily be applied to a mobile electronics consumer market.

In pursuit of this power system, we recognized early on that the human body wastes 80W even during sleep.

WORK RATE	ACTIVITY	WATTS
Very Light (105 to 175 Watts)	Lying on ground	105
	Standing in foxhole	116
	Sitting in truck	116
	Guard duty	137
	Driving truck	163
Light (175 to 325 Watts)	Cleaning rifle	198
	Walking on hard surface @ 1 m/s with no load	210
	Walking on hard surface @ 1 m/s with 20 kg load	255
	Manual of arms	280
	Walking on hard surface @ 1 m/s with 30 kg load	292
Moderate (325 to 500 Watts)	Walking in loose sand @ 1 m/s with no load	326
	Walking on hard surface @ 1.56 m/s with no load	361
	Calisthenics	378
	Walking on hard surface @ 1.56 m/s with 20 kg load	448
	Scouting patrol	454
	Pick and shovel	465
	Crawling with full pack	465
	Foxhole digging	475
	Field assaults	477
Heavy (500 + Watts)	Walking on hard surface @ 1.56 m/s with 30 kg load	507
	Walking on hard surface @ 2.0 m/s with no load	525
	Emplacement digging	540
	Bayonet drill	616
	Walking on hard surface @ 2.25 m/s with no load	637
	Walking on loose sand @ 1.56 m/s with no load	642

Figure 1.3. Waste body heat output for various activities (Warrior Microclimate presentation, Natick Army Center)

In fact, the body outputs over 350 W of waste heat while just walking briskly. If only a fraction of that waste heat could be converted, then the desired 3W power plant may operate directly from the body.

Moreover, this waste heat output is a critical issue for soldier survival. Often times, heat fatigue can occur during soldier activities due to lack of proper ventilation. The garments worn by soldiers are particularly insulative, and as such waste heat is stored in the boundaries of the soldier's outfit. In order to prevent fatigue, waste body heat needs to be removed from the soldier. Any heat engine that harvests waste body heat will also have a microclimate cooling effect.

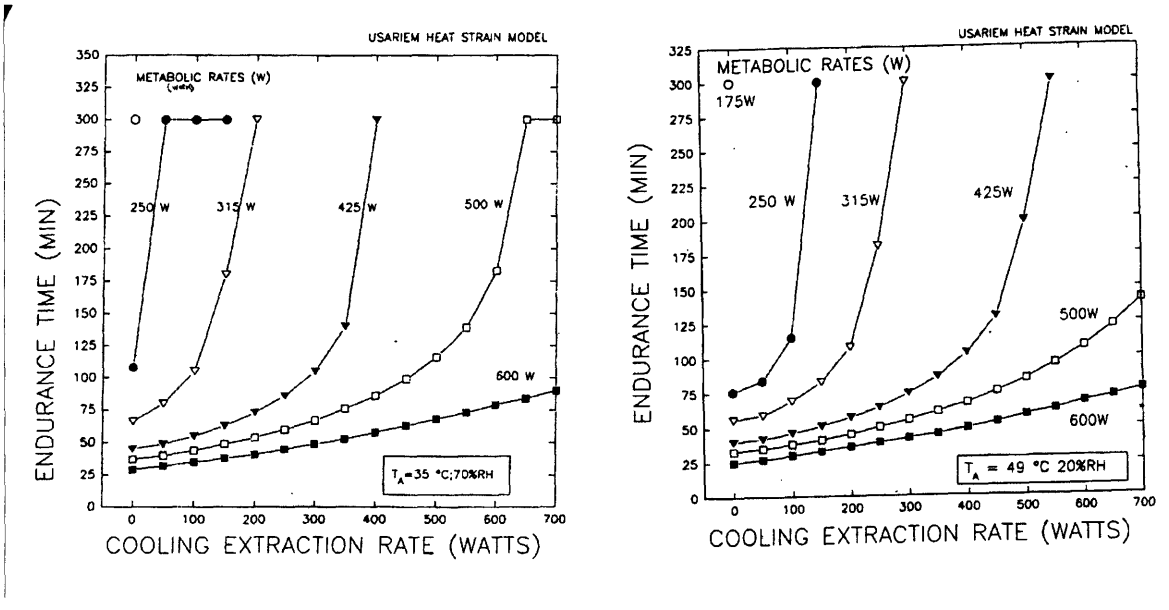

Figure 1.4. Endurance enhancement as a function of microclimate cooling. The soldiers wore the MOPP IV chem./bio warfare suit in this trial. (Warrior Microclimate presentation, Natick Soldier Center)

Most waste body heat is produced at the major muscle groups. Considering the muscle groups within the torso, it is reasonable to assume that nearly a third of waste body heat comes from the back and chest.[7] The body armor vest worn by rifleman provides excellent insulation of these areas, though often causing heat stroke. The torso

is the perfect candidate for waste heat harvesting for two reasons: its output is great and the soldier already wears a garment that insulates the area. A simple plant would absorb heat from between the body armor and torso surface.

Storing this thermal potential in a volatile fluid provides the most effective power transfer to a power conversion device. Except for thermoelectric devices and fuel cells, power converters mainly rely on the motion of a working fluid. We chose a simple Rankine cycle to model our conversion process, and in this case, the liquid stores the thermal energy primarily as enthalpy in the gas phase. An effective power converter then utilizes that enthalpy potential to generate electricity. The exiting high quality two phase mixture flows into a condenser where the parent liquid is reformed. The liquid is then transferred back to the boiler where the process then repeats.

A five month theoretical study showed that waste body heat conversion was only useful in environments with average daily temperatures below 60 degrees Fahrenheit. Despite the temperature limitation, this conversion scheme still has the potential for many applications. The key to the success of this concept, however, is an efficient and simple power converter. The purpose of this report is to expound on the various conversion devices developed in our study, and how they might find further military applications.

Chapter 2: Waste Body Heat Recovery

Three primary methods of energy conversion were considered.

1. Thermoelectric conversion

2. Vortex induced vibration of MEMS piezoelectric cantilevers

3. Magneto-hydrodynamic Rankine cycle

Micro-turbines and fuel cells also have potential in this scheme. Such devices were excluded in our study since considerable work has already been done on their conversion capabilities.

All but the first method rely upon the motion of a gas for electricity production. Thermoelectric devices may utilize thermal conduction by direct integration with the body armor vest. Otherwise, the solid state devices may operate from the convection off a hot gas stream. In all fluid cases a loop heat pipe is employed to produce a high velocity gas from the waste body heat.

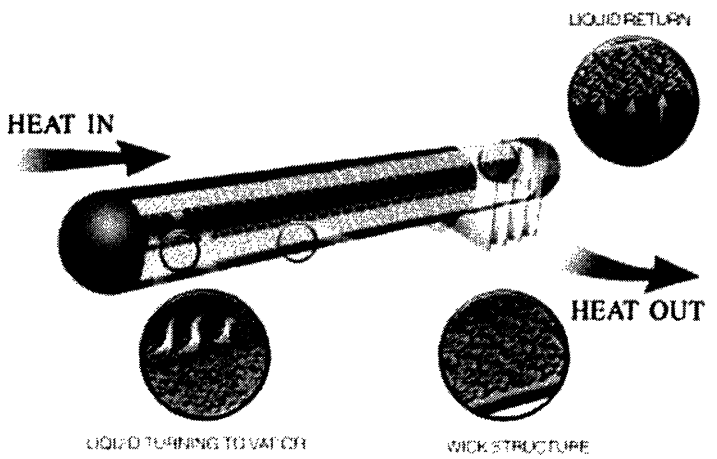

Figure 2.1. Heat pipe schematic courtesy of Thermacore industries

The loop heat pipe is very similar to the conventional heat pipe in figure 2.1. Essentially, a volatile fluid is sealed within a pipe. The fluid is vaporized at the boiler

section, where it then flows at the center of the pipe to the condenser section. Once liquefied, a wicked structure returns the condensate back to the boiler section. A loop heat pipe is exactly the same concept, differing only in that the fluid moves in a pipe loop rather than sealed pipe. In the former, the vapor flows to the condenser through an un-wicked pipe. The condensed liquid is wicked back to the boiler through a pipe segment that contains only the porous wick structure.

The size of these pipes can vary from 1mm to 1 cm inner diameter. Likewise, the pipe can be as much as 2 meters long with negligible heat conduction and viscous losses. The transfer distance is limited by the pressure head produced by the wick structure. Various fluid and wick structure matches exist to accommodate a spectrum of applications.

In any case, the rejection of heat from the condenser into the atmosphere poses a severe limitation to power production. Convection heat transfer typically requires a large surface area or significant temperature differential; such quantities are at a premium in this power scheme. Likewise, the Carnot cycle places a strict limit on maximum thermal efficiency.

$$\eta_c = \left(1 - \frac{T_l}{T_H}\right) \qquad \text{(Eq. 2.1)}$$

At each point of energy conversion and transfer there is an associated temperature drop. Due to real heat transfer processes, the Carnot calculation can not be based off the body and ambient temperatures. In reality, the high temperature reservoir is slightly colder than the body. Likewise, the lower reservoir is warmer than the ambient. The most notable loss attributed to heat transfer is that from convection into the atmosphere.

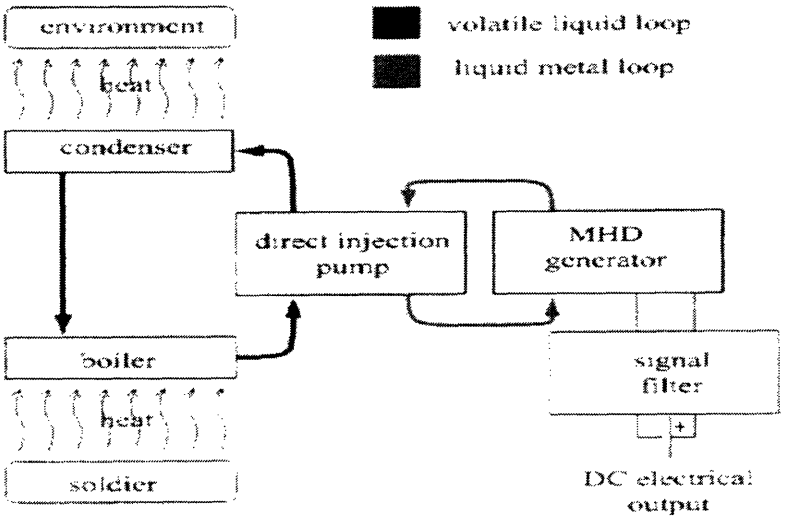

Figure 2.2. Energy flow chart with MHD power plant.

Each volatile fluid interaction results in a temperature drop, and each boxed process has an associated efficiency. The product of the efficiencies provides the mechanical efficiency of the device. Each temperature drop reduces the maximum thermal efficiency. Finally, the product of the mechanical and thermal efficiencies yields the overall conversion efficiency of the device. By tracking the movement of energy across each part of the system we determined what design work could improve the plant efficiency.

The starting assumption was that 1/3 of the waste metabolic heat can be collected from the surface of the torso. Furthermore, we assumed that the soldier loses an average of 500 W of heat over a 16 hour day, and 120 W over the remaining 8 hours. The total average daily power is then 124.4 W. In chapter one, the current time average device power consumption was found to be 1.4 W. Therefore, to meet this power requirement the plant must be at least 1.12% efficient.

At this minimum level, the power plant will be able to recharge the soldier's battery suite. Unfortunately, devices such as the night vision require pulses of power or intermittent high power that exceed 1.4 W. Thus, the plant must either produce more power (for direct use) or be relegated to a re-charge only function; either mode is useful.

A Carnot cycle operating between body heat and ambient temperature extremes provides an upper bound for thermal efficiency of the plant. Since the high temperature reservoir is always at body temperature, 37 degrees Celsius, the highest theoretically allowable ambient temperature for a useful converter is 33.5 degrees Celsius. If the ambient temperature were instead 20 degrees Celsius, our efficiency would at most be 6%. As was shown in the energy diagram, however, conduction and convection temperature losses must be included in the thermal efficiency estimate.

The heat pipe industry designs for a 3 K temperature drop across heat pipes.[8] Convective heat transfer from the condenser requires a larger loss. The heat transfer from the condenser is enhanced by a greater temperature difference between the condenser and ambient. As there is a limited convective surface area available, the convection temperature drop must be optimized to minimize condenser surface area while maintaining efficiency. The worst case scenario is a finned surface cooled by natural convection. For this particular instance we assume the convection surface is the outside of the body armor vest covered with millimeter pin fins, the enhanced area being 1.5 m^2.

$$q = hA(T_a - T_c) \quad \text{(Eq. 2.2)}$$

$$Ra_L = \frac{L^3 \cdot \rho^2 \cdot g \cdot \beta \cdot \Delta T \cdot c_p}{\mu \cdot k} \quad \text{(Eq. 2.3)}$$

$$\overline{Nu}_L = .68 + .513(Ra_L)^{1/4} \cdot (1 + 5.52 \times 10^{-9} \cdot Ra_L)^{1/12} \quad \text{(Eq. 2.4)}$$

Equations 2.2 through 2.4 are Newton's law of cooling, the Rayleigh number and the Nusselt number for turbulent natural convection off a vertical wall. For the small desired temperature differences, the Rayleigh number is $3x10^9$, the convection coefficient is around 21 W/m^2K, and the characteristic length is the mean length of the chest, 0.4 m.[9]

If we wish to generate 3W of useful power from a 124 W source, then nearly 120W must be rejected by the condenser. At the given convection constant and surface area, the temperature drop must be 4 degrees K. The three degrees lost due to heat pipe conduction reduces the effective high temperature reservoir to 34 degrees Celsius. Likewise, if the ambient is already at 20 degrees C, the temperature drop for convection increases the lower reservoir to 24 degrees C. At these corrected temperatures, the maximum thermal efficiency is now 3.26%. The efficiency can be increased by lowering the ambient temperature or increasing the surface area. If the outside temperature is reduced to 15 degrees C, then the thermal efficiency rises to 5.2%.

If we make a conservative estimate that the plant has 50% mechanical efficiency, then the overall efficiency must be at least 2.4% in order to convert 3W of heat. The desired efficiency is not possible above outside temperatures of 15 degrees Celsius (60 degrees F). Considering that the soldier is usually engaged in an activity, we can also assume there will be some forced convection. An increased surface area and forced

convection should make sure that the plant operates properly with small temperature variations about the 15 degrees C critical temperature. This temperature limitation is met by many current military zones for at least 4 months out of the year.

Considering that the army has focused much attention on the area between +/- 30 degrees latitude, the soldier's environment can actually vary from 42 to -5 degrees Celsius. As the ambient temperature rises, the power output of a waste body heat converter drops. Therefore, the true utility of this conversion method depends on the minimum energy needs of the soldier, the mechanical efficiencies of the plant and the external conditions.

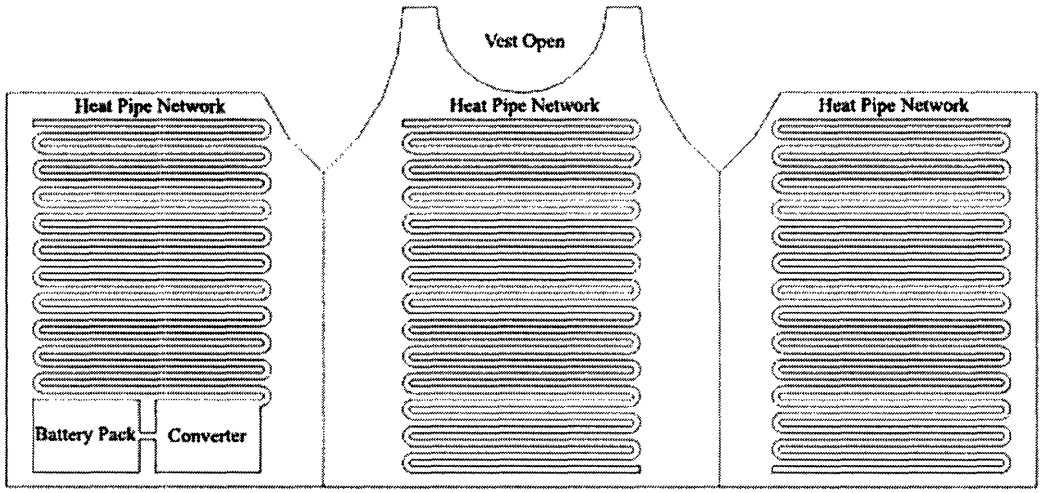

Figure 2.3. Integration of heat pipes, plant and battery pack into the body armor vest.

The design in Figure 2.3 does not require any major alterations of the current garment. Due to power limitations, it is expected that the plant will serve to re-charge the battery suite. The heat pipes have an outer diameter of 3 mm, and mock up versions worn by test subjects remained comfortable to wear. The converter and battery recharge

pack are conveniently located in an existing internal flap of the vest. The insulative nature of the vest provides an ideal location for harvesting waste body heat.

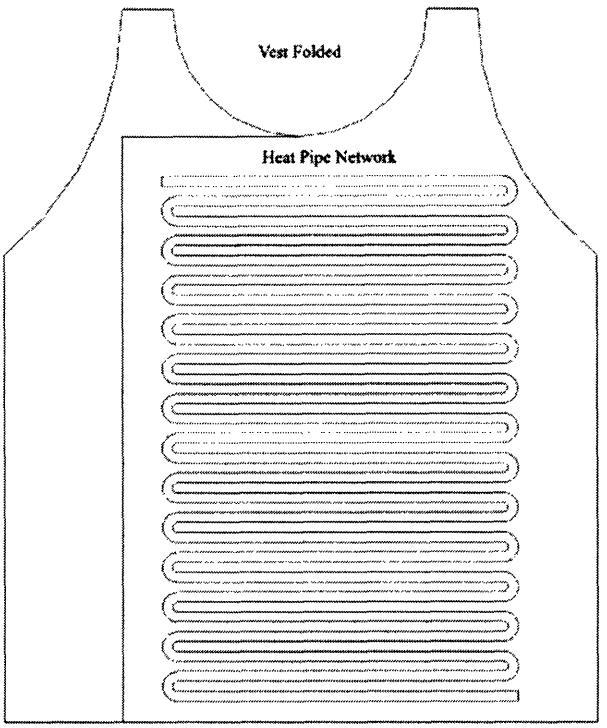

Figure 2.4. Integration of condenser heat pipes with exterior of vest.

The condenser heat pipes are looped on the outside surfaces of the body armor. Despite the picture, these heat pipes are still hidden within the vest, just below the fabric layer. The back of the vest has a matching condenser loop. For product life enhancement the pipes may be integrated into the ceramic armor plate itself. In this way an isothermal convection surface can be formed that also protects the heat pipe structure. These pipes are also only 3mm outer diameter, and may be cast in single compliant sheet. This sheet can be inserted under the fabric of the vest and provide additional protection to the pipes. The integration of the power plant is a complication, as the heat pipes can not be

disassembled. To prevent any poisoning of this sensitive gas system, the entire loop must remain continuous at all times. It is likely that the body armor and power plant manufacturers will have to work together to determine the best design for integration without excessive garment alteration.

The gas evolved in a loop heat pipe (regardless of heat source) is a valid candidate for operating small energy conversion machinery. There are numerous working fluids to choose from, and hence a wide spectrum of operating densities, pressures and flow velocities is available. To date however, heat pipes have still not been applied to any power system. The precision nature of heat pipes may explain this lack of attention.

Heat pipes require very pure gases or gas mixtures, and they fail with any poisoning of the system. The filling and sealing of heat pipes is a chapter of vacuum engineering onto its own. Personal communications with leading manufacturers of heat pipes indicate that incorporation of energy conversion machinery is certainly viable, but has not been studied due to the devotion of industrial research to pure heat pipe science. An effective marriage between power plant and heat pipe requires that the plant does not introduce particulates or detrimental fluids over time.[10]

The MHD and PZT machines in chapters 4 and 5 rely on the gas flow from heat pipes. In the MHD device, the gas is used to pump Mercury through a transverse magnetic field. The motion of this liquid conductor through a transverse magnetic field creates an electric field and a current. The gas pump action is accomplished through surface tension actuated intake and output valves (not pictured in Figure 2.5). The theory and practice behind MHD generator systems is explained in chapter four.

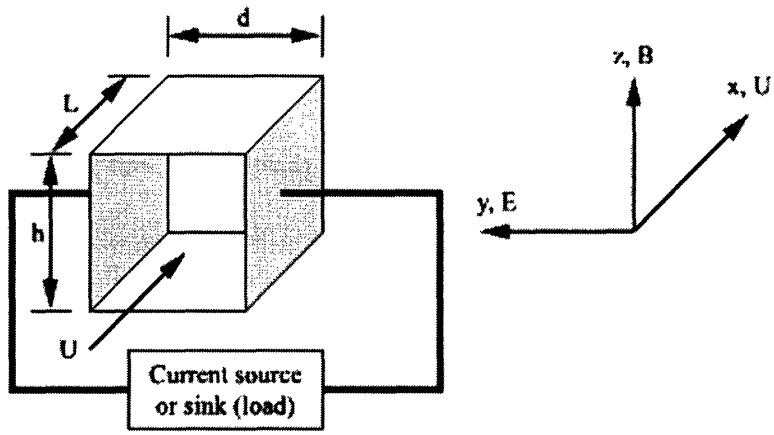

Figure 2.5. MHD device. Axis to the right indicates the direction of flow, electric and applied magnetic field

The advantage of the MHD device is its small scale and ease of production. There exists the potential of creating a network of these generators, as small as dimes, with individual heat pipe loops, while electrically connecting their outputs.

Thermoelectric and vibration energy conversion devices were also examined in the study. Chapter three describes the fundamentals and practice of employing thermoelectric devices as a body heat conversion power plant. Likewise, chapter five elucidates the empirical data behind hydrodynamic wave guides and fluid elastic instability phenomenon. These concepts are put to work in a novel device that extracts energy from a gas flow via vibration of slender elastic piezoelectric members.

---

[1] Energy Efficient Technologies for the Dismounted Soldier, NAS 1997, p. 7
[2] Energy Efficient Technologies for the Dismounted Soldier, NAS 1997, p. 8
[3] Personal Communication, Kailash Shukla, Natick Army Center Engineer
[4] Personal Communication, LTC Charles Dean, ISN Army Liason
[5] Personal Communication, Kailash Shukla, Natick Army Center Engineer
[6] America Online news Publication, December 2003
[7] Personal Communication, Brad Laprise, Natick Army Center Engineer
[8] Personal Communication, Fred Philips, Thermacore Engineer
[9] Personal Communication, Brad Laprise, Natick Army Center Engineer
[10] Personal Communication, Fred Philips, Thermacore Engineer

Chapter 3: Thermoelectric Energy Conversion

A study was performed to determine if thermoelectric devices could convert waste metabolic heat into useful electricity. The study documented the basic governing physics and the industry state of the art for thermoelectric converters as well as compared modern approaches with the desired scope of this analysis. The purpose of the study was to determine if thermoelectric devices were a viable conversion platform for waste body heat recovery.

A thermoelectric method of converting heat to electricity or electricity to heat is defined when heat is used to elevate the energy of bound electrons in a solid thereby generating electricity (or vice versa). This approach should not be confused with thermoionics, which deals with the elevation of free (instead of bound) electrons in a solid to produce power. Thermoelectric power generation features the unique trait of requiring no moving parts for operation. This advantage of working entirely in the solid state, "allows the design for potentially very reliable electric power production means over a long service life".[1] Considering this huge advantage, is the thermoelectric approach right for converting waste metabolic heat into useful and useable amounts of energy?

Before an answer to that question is presented, the physical characteristics and relationships associated with thermoelectric devices needs to be expounded.

Metals and semiconductors have different bands of electrons. In the conduction band, bound electrons are found. However, in addition to the bound electrons, "holes," i.e.: electron deficiencies are also present. "Holes" are free to move around in the conduction band of metals and semiconductors. In the presence of an electric field, these

electrons and electron deficiencies are motivated and can establish a current or flux of charges. Similarly, if the electrons are exposed to a temperature gradient, a flux of charges is also observed.

To begin quantifying the physical phenomena, a bar, *a*, of conducting material is coupled by two wires of a material *b* to a means of measuring voltage. This apparatus is depicted on the left side of Fig. 3.1.

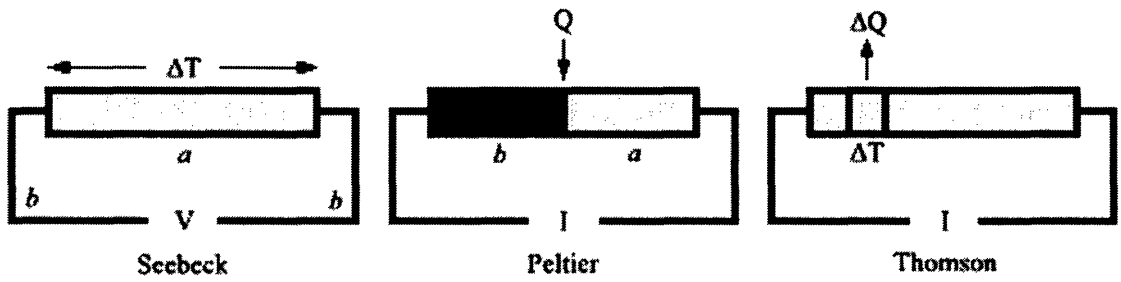

Figure 3.1. Fundamental thermoelectric effect experiments. (Decher, p. 241)

If both ends of *a* are maintained at two different temperatures, $\Delta T = T_1 - T_2$ for example, Seebeck (1822) observed "that a voltage V (which varies with ΔT) can be measured when the current is zero".[2] The proportionality constant's limiting value of the junction *a-b* is termed the Seebeck coefficient, α :

$$\alpha_{ab} \equiv \lim_{\Delta T \to 0} \left(\frac{\Delta V}{\Delta T} \right) \text{ or } V = \int_{T_1}^{T_2} \alpha_{ab} dT \qquad \text{(Eq. 3.1)}$$

The integral form of Eq. 3.1 states that "electrons will acquire an electric potential as electrons are transported from a region of varying thermal energies as measured by their temperatures".[3]

Next, consider a current source connected to an apparatus of two materials, say *a* and *b*, as arranged like shown in the center of Fig. 3.1. Peltier (1844) observed that "the current flow results in the evolution of heat in an amount proportional to the current and that heat is absorbed when the direction of the current is reversed",[4] which is also known as the *Peltier effect*. The Peltier coefficient, π, is defined as the ratio of the heat in respect to the current passing through the junction of the two materials:

$$\pi_{ab} \equiv \left(\frac{Q}{I}\right) \qquad \text{(Eq. 3.2)}$$

Following Peltier, Thomson (Lord Kelvin, 1854) discovered that "a unit length of bar with a temperature gradient [shown on the right side of Fig. 3.1] evolves heat (in excess of the joule dissipation = I^2R) when current flows".[5] Hence, the Thomson coefficient, γ, is defined though the ratio:

$$\gamma \equiv \lim_{\Delta T \to 0} \frac{1}{I}\left(\frac{\Delta Q}{\Delta T}\right) \text{ or } Q = \int_{T_1}^{T_2} \gamma dT \qquad \text{(Eq. 3.3)}$$

With these three relationships and their core constituents, α, π and γ, an energy balance can be created that must govern the thermoelectric effect of a circuit illustrated in Fig 3.2.

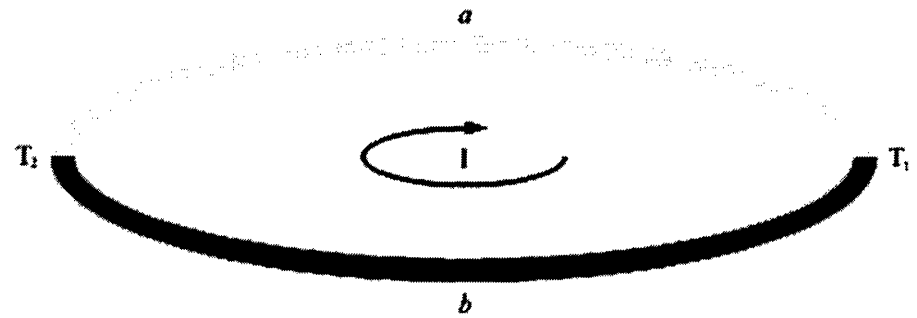

Figure 3.2. A simple, isolated thermoelectric circuit of two dissimilar materials, *a* and *b*. (Decher, p. 242)

The balance dictates the electrical power produced from the temperature difference sustained across a junction is equal to the change in heat seen at the two junctions and across the two bars. Consequently,

$$\int_{T_1}^{T_2} \alpha_{ab} I dT = \left(\pi_{ab_2} - \pi_{ab_1}\right) I + \int_{T_1}^{T_2} \left(\gamma_a - \gamma_b\right) I dT \qquad \text{(Eq. 3.4)}$$

which, differentiated is,

$$\alpha_{ab} = \frac{d\pi_{ab}}{dT} + \left(\gamma_a - \gamma_b\right) \qquad \text{(Eq. 3.5)}$$

If the electrothermal device's process is reversible, another relationship between the Seebeck, Peltier and Thomson coefficients can be established. This "assumption is borne out experimentally and results in the requirement that the entropy production rate for the system in [Fig. 3.2] be zero".[6] Thus, the entropy created, ΔS, at the two junctions of the dissimilar materials due to the difference in temperatures is observed to be

$$\Delta S = \left(\frac{\pi_{ab_2}}{T_2} - \frac{\pi_{ab_1}}{T_1}\right) I \text{ or } dS = I d\left(\frac{\pi_{ab}}{T}\right) \qquad \text{(Eq. 3.6)}$$

Thus

$$\int_{T_1}^{T_2} I d\left(\frac{\pi_{ab}}{T}\right) + \int_{T_1}^{T_2} I \frac{\left(\gamma_a - \gamma_b\right)}{T} dT = 0 \qquad \text{(Eq. 3.7)}$$

or, in differential form,

$$\frac{d\pi_{ab}}{dT} - \frac{\pi_{ab}}{T} + \left(\gamma_a - \gamma_b\right) = 0 \qquad \text{(Eq. 3.8)}$$

Substituting Eq. 3.5 into Eq. 3.8 offers an insight into the relationship between the Seebeck, α, and Peltier, π, coefficients:

$$\alpha_{ab} = \frac{\pi_{ab}}{T} \qquad \text{(Eq. 3.9)}$$

With additional calculation, a relation of the Thomson coefficient, γ, with either of the other two can be achieved. However, in thermoelectric "generators of practical interest, the effects of phenomena controlled by the Thomson coefficient are generally small (because the temperature gradients are small) so they are not considered further".[7]

Additionally, it turns out that the Seebeck effect is minimal in metals. So instead of using metal material, semiconductors are employed because of the nature of the Seebeck effect being up to two orders of magnitude greater. Aside from material choice, the thermoelectric physical phenomena also dictate that the trade-off for thermoelectric devices being able to work entirely in the solid state is that they suffer from minimal thermal efficiencies. According to Decher (1997),

> "One may conclude that the advantage of simple and potentially very reliable thermoelectric systems must be balanced with relatively low thermal efficiency. The load resistances for maximum power and maximum efficiency are not far from one another. The efficiency at maximum power is not much less than its absolute maximum. The power output is scaled directly by the magnitude of the Seebeck effect voltage (squared), which can be established for chosen materials. A small electrical resistance of the semiconductor helps to increase power, although this is not a property that can be readily manipulated."[8]

That "the load resistances for maximum power and maximum efficiency are not far from one another" and other similar thermoelectric effect advantages exist have established that this approach could possibly be a feasible method for converting waste metabolic heat into useful ad useable amounts of energy. One such modern thermoelectric device, an AMTEC (Alkali metal thermoelectric conversion) converter exhibits such attributes as a current density of the order of 1 A/cm^2 and a working efficiency of up to 15%.[9] However in order to achieve such a high efficiency (thermoelectricity-wise), temperature

differences, ΔT, are needed to be an order (or two) of magnitude higher than what would be expected in a waste metabolic heat/atmospheric temperature environment.

To iterate, it has been established that if a temperature gradient is placed across the junctions of two dissimilar conductors, electrical current will be the result (Seebeck), and that if a current is passed through two dissimilar conductors, a heat flux will be seen in the form of either emission or absorption at the junctions of the materials (Peltier).[10]

The application of the thermoelectric physics has led to the growing thermoelectric industry, with Seebeck's and Peltier's work as its foundation. However, although their work occurred in the early ninetieth century, the fruits of their labor only came into existence with the mid-twentieth century's development of the semiconductor. Whereas thermoelectric tests using metals only resulted in thermoelectric efficiencies in the fractions of a percent, the late twentieth century's semiconductor technologies have given rise to the more modest efficiencies of up to 15%, as stated previously. Modern thermoelectric devices can reliably work as solid-state heat pumps (for either heating or cooling) or as solid-state DC generators.

For ease of manufacturability and to be able to "combine" the capabilities of multiple thermoelectric devices, thermoelectric "modules" are a common product on the market today. "A typical thermoelectric module consists of an array of semiconductor pellets of Bismuth Telluride that have been 'doped' so that one type of charge carrier—either positive or negative—carries the majority of the current."[11] The pellets are arranged in a manner that connects them electrically in series but thermally in parallel. The platform for which the pellets and their connecting conductive tabs reside on is made of metalized ceramic substrates. This assembly forms a layer and its dimensions can

range from less than a quarter of an inch squared to about two inches squared. Layer modules can work alone or in groups with either series, parallel or dual series/parallel electrical connections.[12]

To employ a thermoelectric module to generate (DC) power, a temperature gradient is created across the device. Electrical current will be established if a load is connected to the thermoelectric generator. Today, most thermoelectric generators are utilized to provide power for remote telecommunication, navigation, and petroleum installations.[13] However, more common commercial energy conversion and even space systems abound.

Lastly, of note is that thermoelectric devices are cheap to produce. A typical thermoelectric module costs in order of $10 to $100 to manufacture.

Even with its advantages of requiring no moving parts, existing in modular and stackable forms, and being inexpensive and easy to produce, thermoelectric devices are not the optimal choice for converting waste body heat into electricity. The obstruction keeping modern thermoelectric methods from becoming an effective metabolic heat conversion tool is known as the thermoelectric "sweet spot," as illustrated in Fig.3.3. This "sweet spot" is a span of operating differences in temperatures, ΔT, compared with the device load. Furthermore, "ninety percent of all practical applications for thermoelectric technology fall within [this] very narrow range of operating conditions."[14] Characteristics indicative of this "very narrow range," include a ΔT between 30°C and 50°C, load current draw between 70% and 80% of the device's maximum current and a coefficient of performance (COP) between 0.25 and 0.4.[15] A waste metabolic heat conversion device would typically require a temperature difference, ΔT, of half an order

of magnitude smaller than what a thermoelectric device could handle due to the "sweet spot" limitation. Apropos, modern thermoelectric technology does not position thermoelectrics as an effective method for a waste body heat to electricity conversion device.

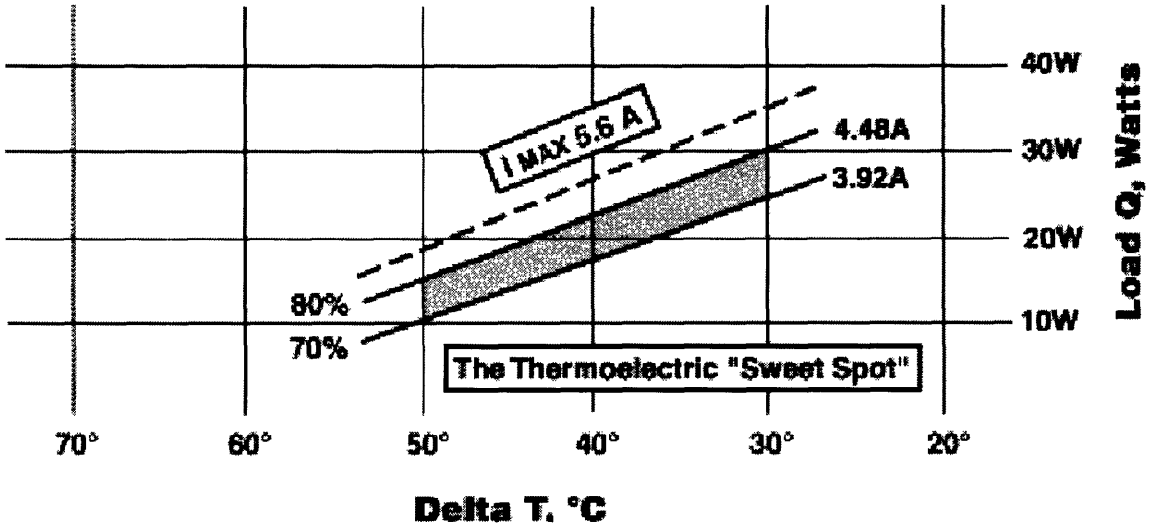

Figure 3.3. The Thermoelectric "Sweet Spot." (An Introduction to Thermoelectrics, p. 5)

---

[1] Decher, R. (1997). Direct Energy Conversion. New York, NY: Oxford University Press. p. 134.
[2] ibid. p. 240
[3] ibid. p. 240
[4] ibid. p. 241
[5] ibid. p. 241
[6] ibid. p. 242
[7] ibid. p. 242
[8] ibid. p. 248
[9] ibid. p. 251
[10] An Introduction to Thermoelectrics. (2002): Tellurex Corporation. p. 1
[11] ibid. p. 1
[12] ibid. p. 1
[13] ibid. p. 2
[14] ibid. p. 5
[15] ibid. p. 5

Chapter 4: Magneto Hydrodynamic Energy Conversion Design Experiment

Magneto hydrodynamic energy conversion is a unique concept that has not proliferated the power conversion technologies market. The theory of MHD dates back to Farady who tried to use it in calculating the flow speed of the Thames. Shercliff, Hughes and Branover are primarily responsible for its growth in the 20th century. The greatest advances in MHD technology were made in the 1960's and 70's when MHD was coupled with solar power. To date, its only commercial power application exists with some coal burning power plants; the hot combustion gases are ionized and pass through a magneto plasmadynamic crossed fields device to improve the overall output of the plant. The exit stream of the MHD generator is then fed into a conventional turbine.

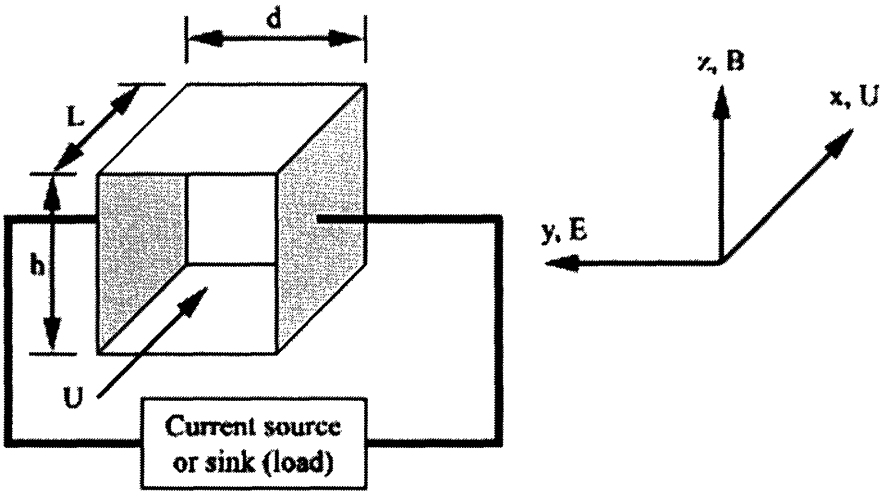

Figure 4.1. MHD crossed fields device. Axis to the right indicate the direction of velocity, electric and applied magnetic fields. (Decher, p. 27)

The theory of MHD operation is contained in Appendix A. The primary limitation of large scale MHD generators is the creation of high inductions fields within large pipes. Typically, industrial MHD machines employ superconducting coils to produce the necessary fields for operation. At the very small scale however, powerful

fields can be produced with relative ease. At the small scale, geometry based limitations on MHD generators are eliminated. Appendix A provides analytical solutions for the optimal short circuit current and open circuit voltage. These properties as well as expected efficiency are given as functions of flow geometry and speed, internal resistance and load resistance.

Theoretically, MHD generators can be highly efficient and simple to fabricate. Their utility as a power plant, however, is limited by the motivation of liquid metal through the crossed field section. An effective pump mechanism must be included to move this secondary working fluid. To date, we have not found a pump that operates off a gas stream at efficiencies applicable to waste body heat conversion. Whereas theoretically this conversion method stands to be very effective, it is severely limited by the low efficiency and lack of vapor operated liquid metal pumps.

An experimental apparatus consisting of a magneto hydrodynamic channel, a pair of bar electrodes, a magnetic field, a liquid metal, a means of pumping the liquid metal, and a method to measure the voltage drop across the magneto hydrodynamic channel were required to test the workability of practical magneto hydrodynamics on the scale desired. During the research, a total of three magneto hydrodynamic channels were designed, built and tested. All three failed to produce the result that was needed to place magneto hydrodynamics as a feasible means to convert waste metabolic heat into useable and useful amounts electricity. However, although no significant results could be obtained from the three designs, the knowledge gained from each apparatus's flaws was instrumental in evolving the magneto hydrodynamic channel design. Figure 4.2 compares the sizes and shapes of the three generations of magneto hydrodynamic channel

designs and offers insight into the design evolution process involved. Pictures of the magneto hydrodynamic channels are contained in Appendix B.

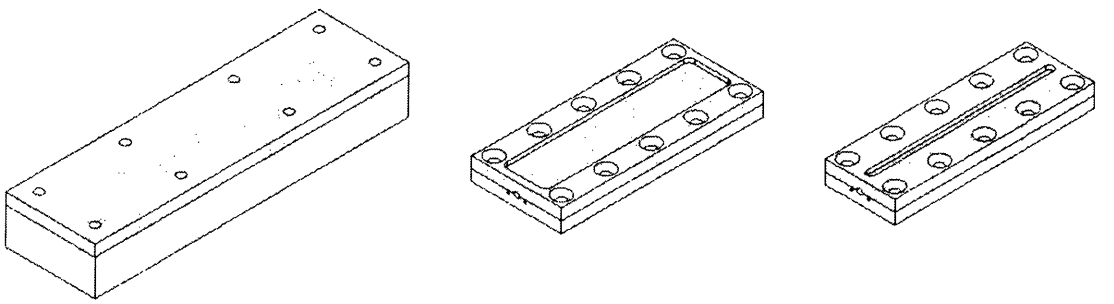

Figure 4.2. Magneto hydrodynamic channel design generations and evolution with the earliest (and largest) starting on the left.

The initial design requirements for the channel were that it had to be able to handle a sealed canal of a pressurized magneto hydrodynamic fluid, house the bar electrodes and be inert with the current and magnetic flux, and be able to link with a fluid supply, waste reservoir and voltage reader. The manufacturing requirements called for an apparatus that could be built and afforded by a student.

After some apparatus planning, it was discovered that it was highly desirable for the channel to also be viewable from the outside to ensure that the magneto hydrodynamic fluid was flowing properly. This ability was added to the list of the magneto hydrodynamic channel's requirements.

To construct the apparatus within the design and manufacturing constraints, the ideal materials were first selected. The magneto hydrodynamic channel itself would be made out of LEXAN, a nonconductive polycarbonate that is available transparent and possesses a yield strength of 62.1 MPa. LEXAN was immediately available as scrap

from various MIT machine shops and, if needed, could be bought at a very reasonable price. The maximum channel pressure that the LEXAN would experience during experimentation was estimated at 60 kPa, which was well within mechanical limits. The LEXAN would also be inert in the presence of a magneto hydrodynamic fluid, the electrodes, and the magnetic flux the channel would experience. Copper was identified as the best electrode material due to its inexpensive cost, availability and high electrical conductivity. Neodymium Iron Boron magnets were acquired which would allow for up to 1.2 Tesla to be directed through the magneto hydrodynamic channel.

For the working fluid, mercury was obtained. Mercury, a liquid metal, is a good choice because of its chemical inertness, conductivity, and magneto hydrodynamic properties.

The first design of the magneto hydrodynamic channel incorporated two different sizes of LEXAN plate material, with the entirety of the channel itself milled out of the larger plate. An image of the first generation (G1) magneto hydrodynamic channel is shown in Figure 4.3. The same model is shown in an exploded view in Fig 4.4. Detailed part drawings for the G1 channel are contained in Appendix C. For ease of manufacture, the first magneto hydrodynamic channel had the channel itself in a large (0.8 inch thick) LEXAN plate so as not to create two possibly mismatching milled channel pockets. The top plate, which served as the channel cover, was obtained at 0.25 inches thick. Both the top and bottom plates also featured milled pockets for the electrodes. It should be noted, however, that two sets of double-stacked copper bars were used as electrodes because of the machine tools and copper plate thickness available.

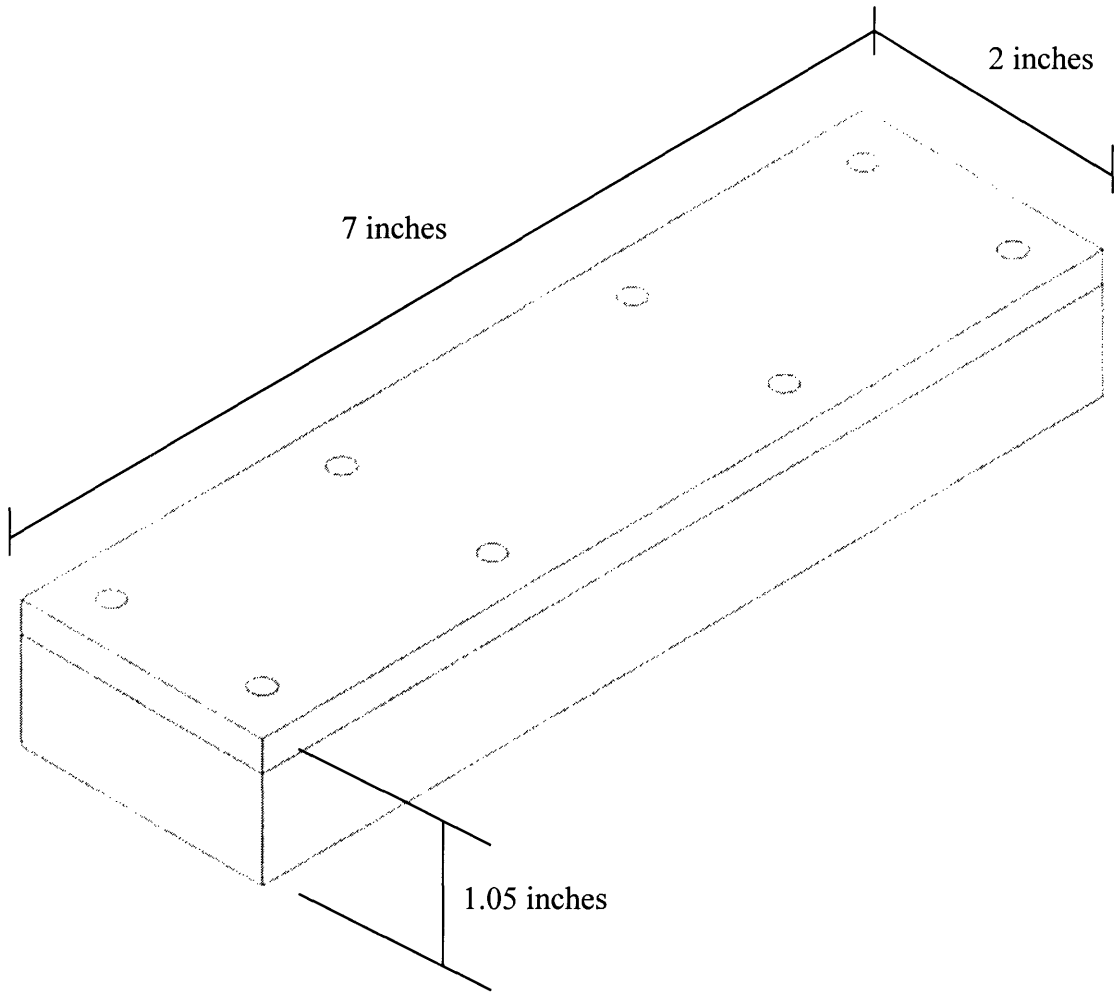

Figure 4.3. First generation magneto hydrodynamic channel.

Short strips of copper were also used as electrode leads. The working fluid in the G1 magneto hydrodynamic channel employed an inlet and an outlet set at right angles to the channel itself for ease of manufacture. Plastic tubing and connectors joined the inlet and outlet to the pump and working fluid receptacle, respectively. A total of eight common steel machine screws and nuts were used to fasten the top and bottom plates together. Lastly, Devcon 5 Minute Epoxy was applied to ensure a sealed device.

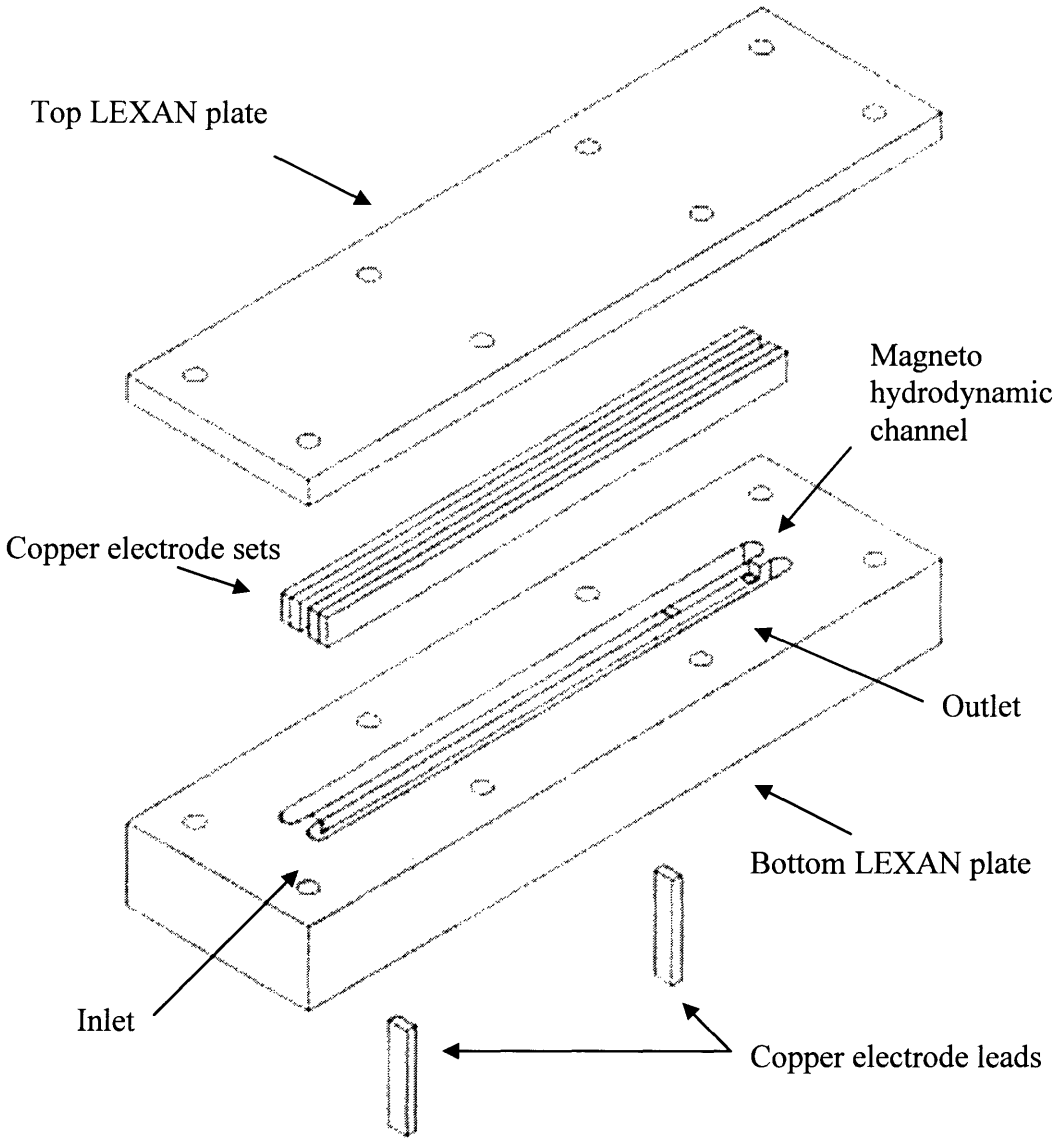

Figure 4.4. Exploded view of the first generation magneto hydrodynamic channel.

The size of the magneto hydrodynamic channel in this first apparatus was 4.84 inches by 0.118 inches squared. These channel dimensions corresponded to 123mm by 3 mm squared, which had been obtained theoretically as desirable channel proportions for the scope intended.

The first generation magneto hydrodynamic channel only produced voltages in the tens of millivolts (0.1 and 0.2 millivolts) during 10 mL/s mercury flow and in the presence of 1.2 T; theory predicted a result of at least 100 millivolts. These results were possibly the product of design mistakes. As a design oversight, when the Neodymium Iron Boron magnets were placed above and below the channel, they were too far way from the channel for it to receive sufficient magnetic flux. They also collided with the machine screw heads, and were not allowed to be equidistantly separated from the channel. The inlet and outlet tubing position also interfered with the magnets.

The first design revision was seen with the G2 magneto hydrodynamic channel, as shown in Figure 4.5, and, exploded, in Figure 4.6. The largest change in the G2 was the choice in making the top and bottom plates entirely symmetric except for the machine screw countersinks and counterbores and the new copper wire lead holes. The new LEXAN plate thickness used was 0.25 inches (the same as the G1's cover thickness). Additionally, it was revealed that if the magnetic flux was concentrated solely through the magneto hydrodynamic channel, it would have beneficial stability effects in the flow as well as nearly doubling the magnetic flux up to 2 T. To concentrate the flux, a magnetic flux focuser was designed and built with the G2 in mind. Figure 4.7 illustrates how low-grade M54 Steel, an extremely high magnetic conductor, was employed to focus the magnetic flux through the G2's magneto hydrodynamic channel and then have it wrap around the G2, completing a magnetic circuit. Based on the theory that as long as the narrowest part of the magnetic circuit's cross-sectional area was sent through the channel, the channel would experience the peak flux of the magnetic circuit. An exploded view of just the magnetic flux focuser is depicted in Figure 4.8.

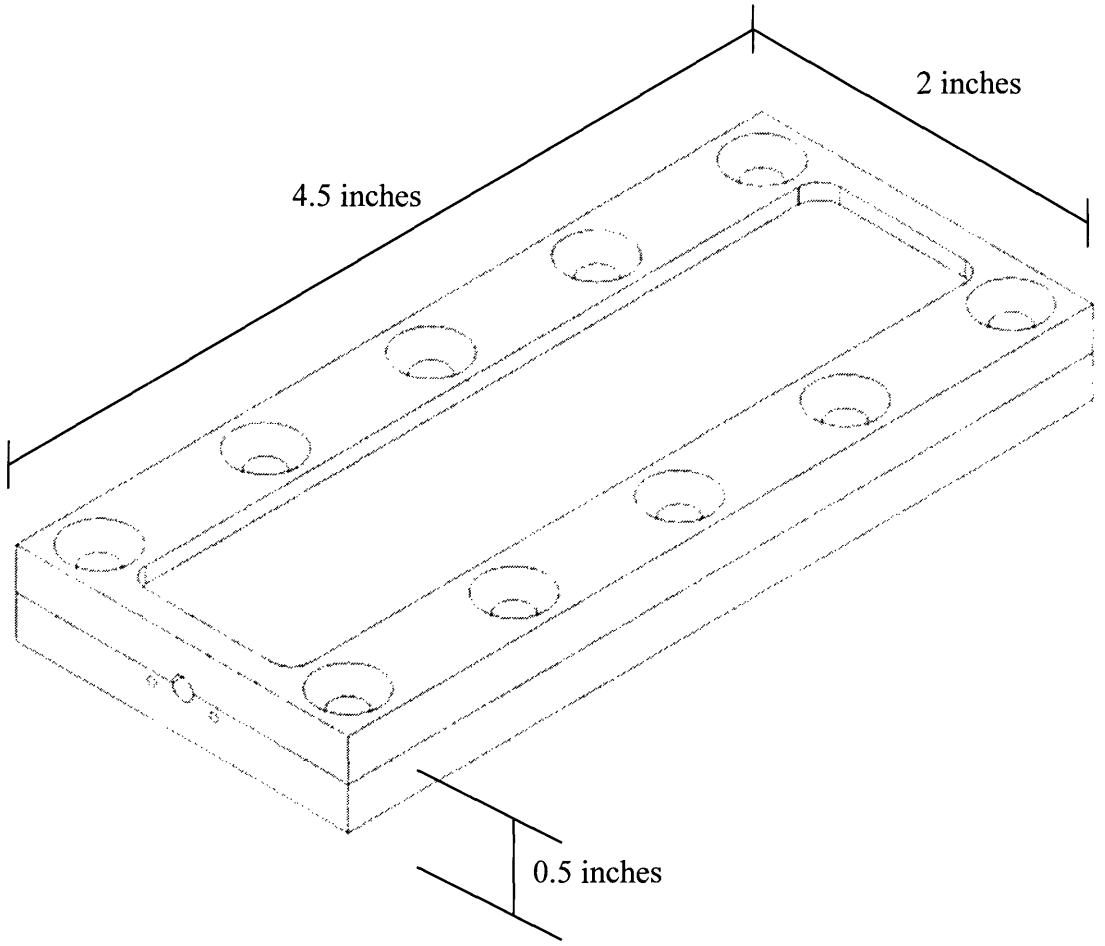

Figure 4.5. Second-generation magneto hydrodynamic channel.

To not interfere with the focuser, new machine screw and nut material needed to be selected. Type 316 Stainless Steel was identified as an ideal choice as strong steel that exhibited strong nonmagnetic properties—perfect for not disturbing the focuser's effect.

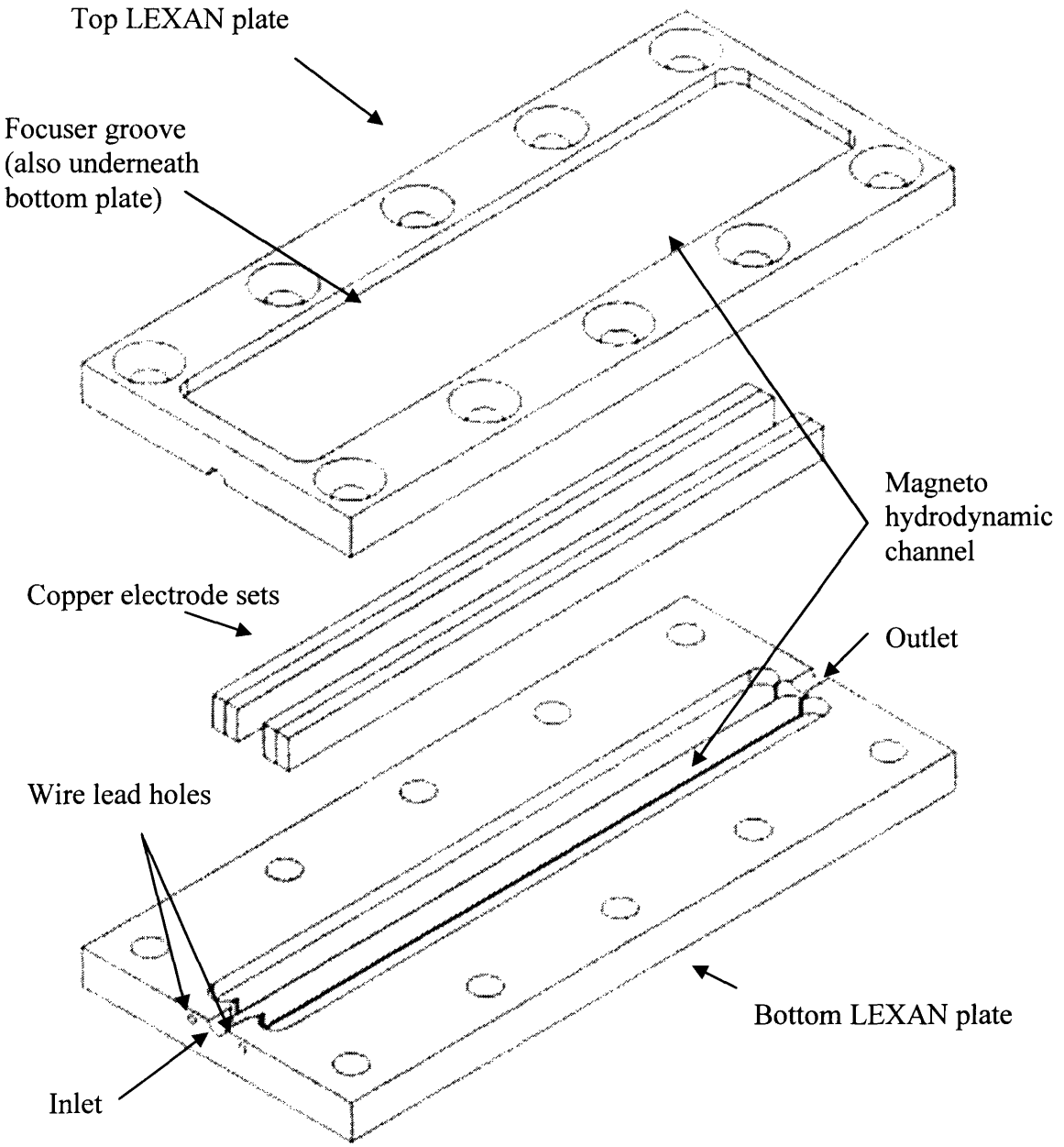

Figure 4.6. Exploded view of the second-generation magneto hydrodynamic channel.

With the focuser occupying space immediately above and below the magneto hydrodynamic channel, the channel inlet, outlet and the electrode leads were moved to the sides. The same tubing and tube connector types that were used in the G1 were also

used in the G2. Also, to allow for the angled parts of the focuser to be only 0.0625 inches (1/16 of an inch) away from the channel itself, material was removed from the top of the top LEXAN plate and from the bottom of the bottom plate.

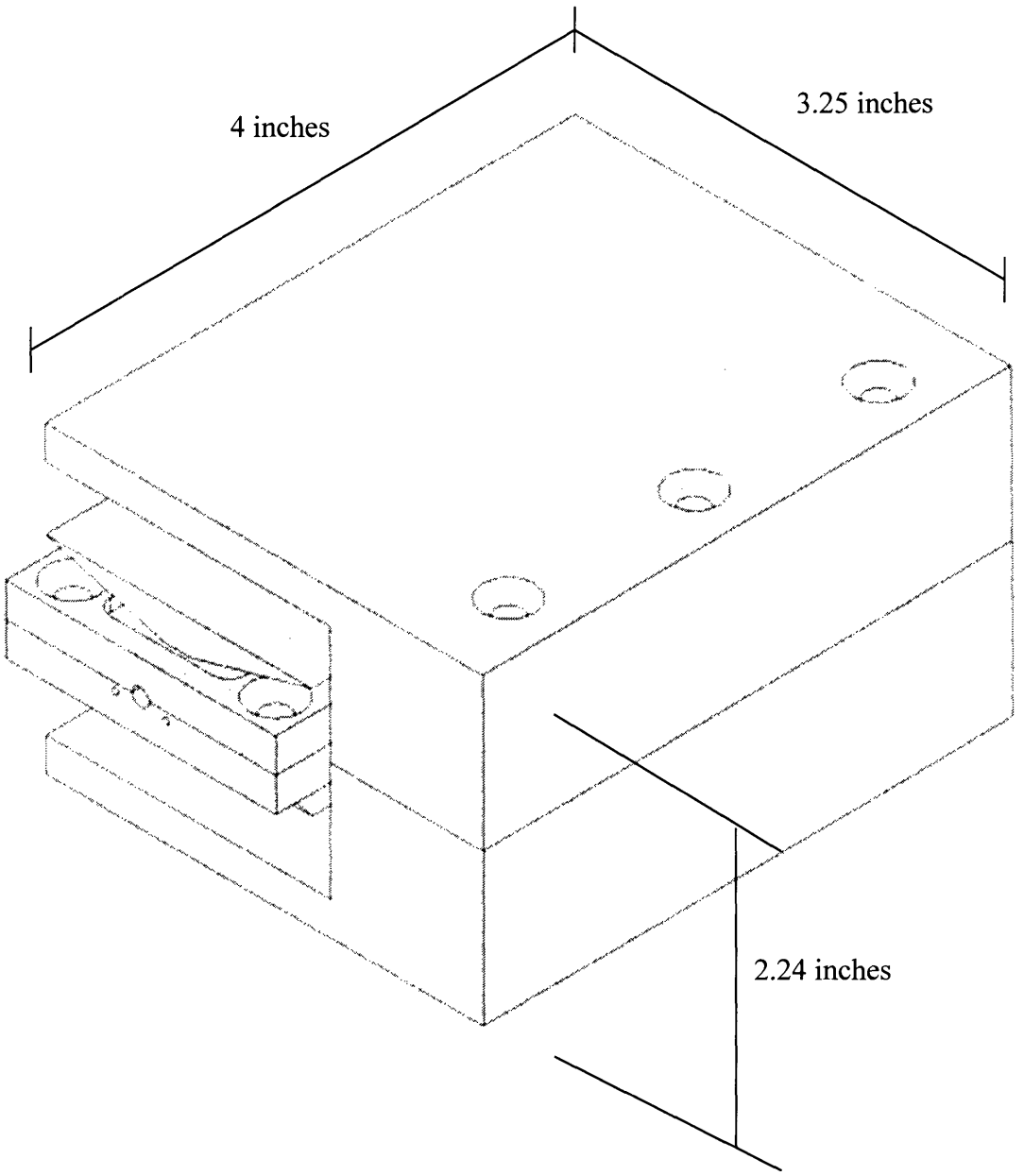

Figure 4.7. Second-generation magneto hydrodynamic channel shown with supplemental magnetic flux focuser.

0.0625 inches was discovered experimentally as the thickest the LEXAN plate could be shaved to while still maintaining its deflection strength.

For the G2, the magneto hydrodynamic channel's dimensions were revised to 4 inches by 0.1875 inches squared (3/16 of an inch squared). These new dimensions were products of optimization with both the magneto hydrodynamic theory and part manufacturability in consideration.

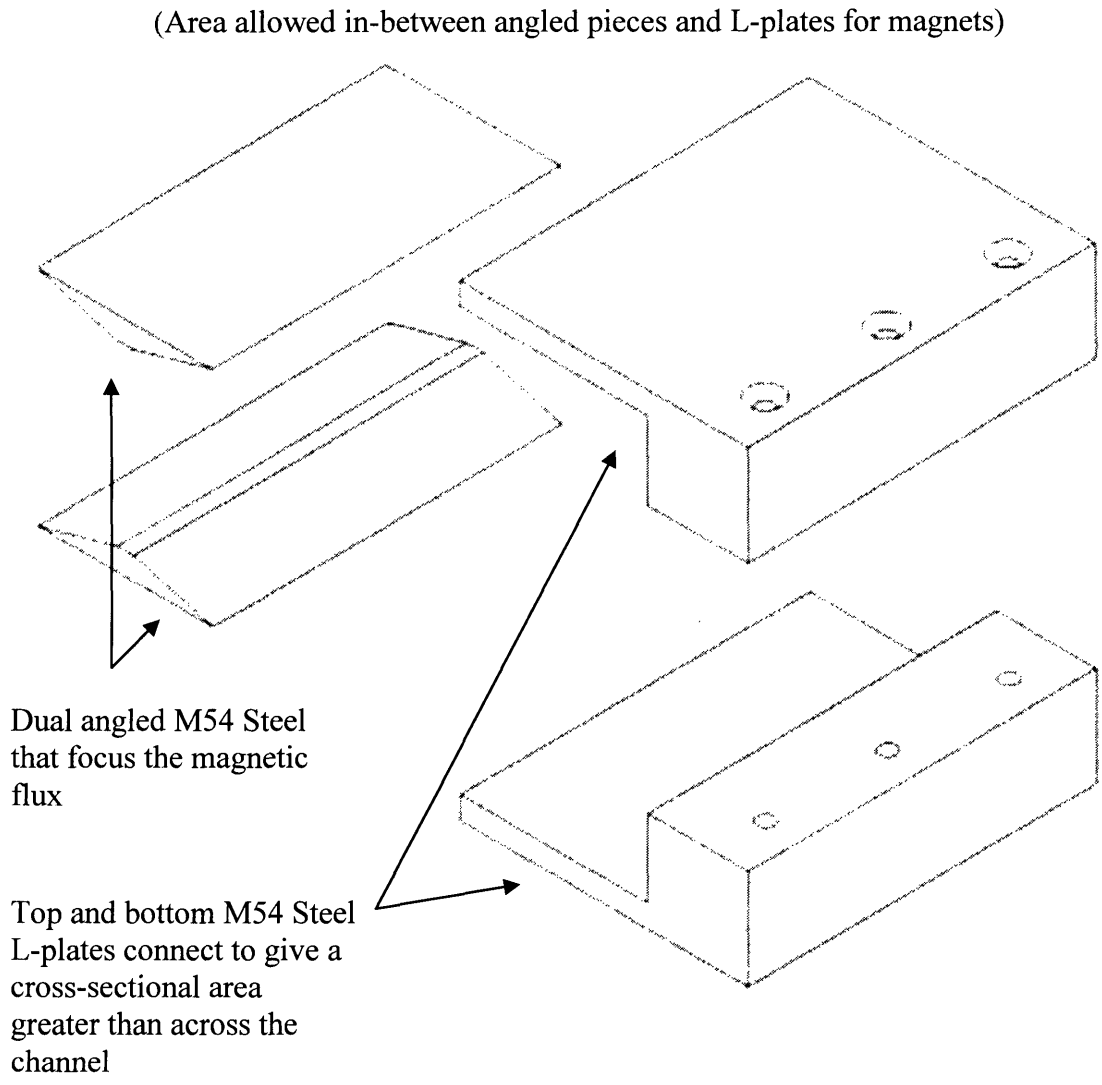

Figure 4.8. Exploded view of the magnetic flux focuser.

Part drawings for the second-generation magneto hydrodynamic channel and the magnetic flux focuser are located in Appendix C.

The second-generation magneto hydrodynamic channel also failed to produce the results desired to make it a feasible process for the purpose intended. The G2 exhibited test result voltages in the tens of millivolts (0.1 and 0.2 millivolts) with 10 mL/s of mercury flow (just like the G1) and in the presence of 2 T. However, the G2 also had its share of manufacturing flaws. It is believed that the machine used to mill the G2 LEXAN plates suffered from inaccurate internal backlash. Consequently, when the G2 was being assembled minor discrepancies were observed in the mating of the top and bottom plates. Because the G2 experienced significant leaks when the mercury was sent through the channel, minor manufacturing flaws or inaccuracies were the most likely culprit. Design flaws in the G2 included the fact that the wire leads should have been cut halfway into each plate instead of just through one to make the soldering work a lot easier, not enough depth difference was given between the channel and electrode slots, and less LEXAN material area-wise needed to be removed from the plates.

The second design revision for the test apparatus was embodied in the G3. Figure 4.9 displays the third generation magneto hydrodynamic channel. Figure 4.10 has the G3 in exploded view. Change was minimal in the transition from the G2 to the G3. Nevertheless, the G2's primary design flaws were fixed in the G3. These flaws included the wire lead hole locations being moved onto the plane of the channel, greater depth difference between the electrode pockets and the channel, and the use of just one direct slot for the magnetic flux focuser instead of an area pocket. Unlike the significant size

difference between the G1 and the G2, the size difference seen between the G2 and the G3 was little, reflecting the many similar aspects between the G2 and the G3. The third generation magneto hydrodynamic channel was also made with the existing magnetic flux focuser in mind, and when completed, was connected to it. However, to save a noteworthy amount of manufacturing time, the G3's single top and bottom slots called for the angled M54 Steel pieces to have material be removed from their tips. This was a big manufacturing advantage because cutting away a little of the M54 Steel in the angled pieces required significantly less time than two area pockets in the LEXAN plates.

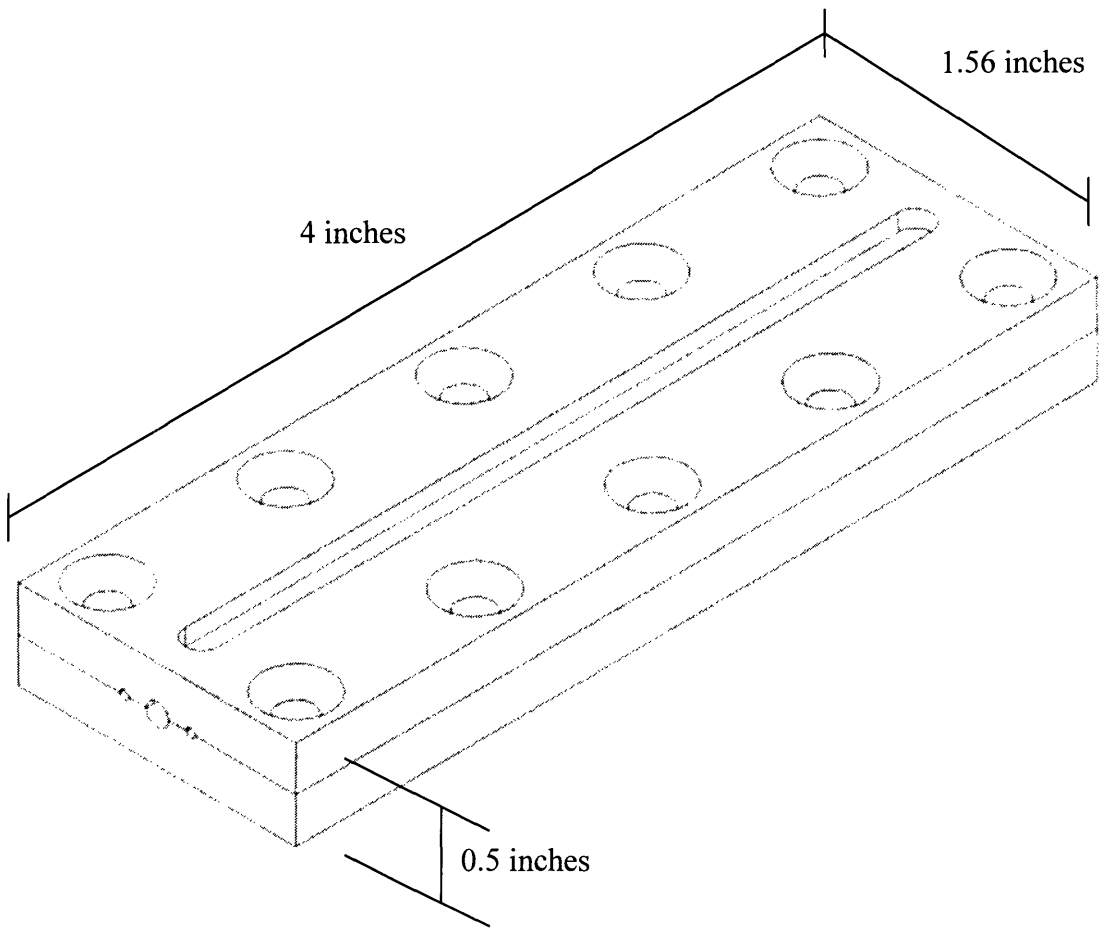

Figure 4.9. Third generation magneto hydrodynamic channel.

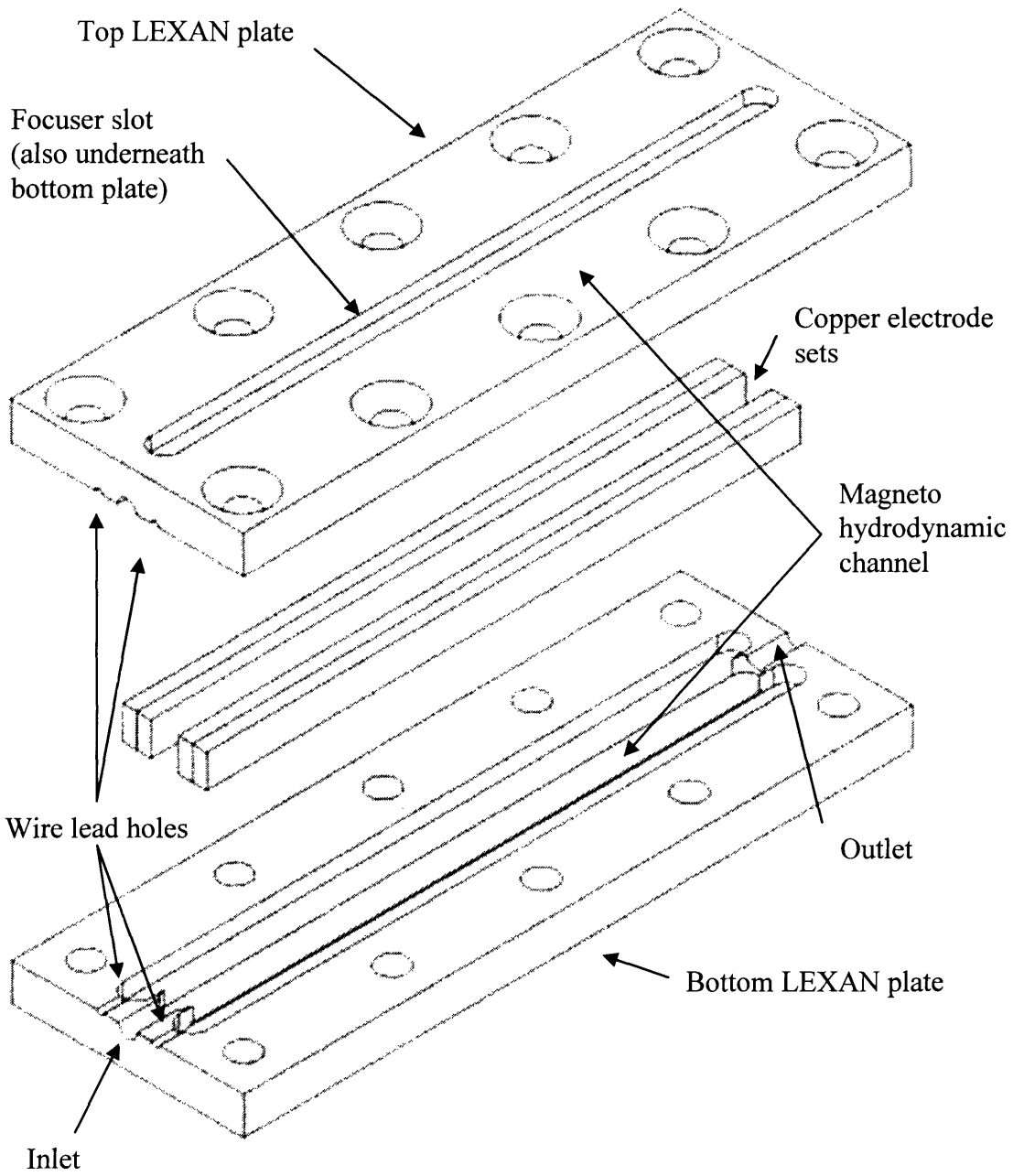

Figure 4.10. Exploded view of the third generation magneto hydrodynamic channel.

The magneto hydrodynamic channel's dimensions in the G3 were the same as the G2—4 inches by 0.1875 inches squared (3/16 of an inch squared). Part drawings and details for the G3 magneto hydrodynamic channel and the minor magnetic flux focuser revision for the G3 are found in Appendix C.

The G3, which was the final design of the magneto hydrodynamic channel, produced 0.5 millivolts as its peak output when 10 mL/s of mercury was passed through it. Like the test with the G2, the G3's channel was also subjected to the boosted 2 T field.

All three designs only produced voltages in the tens of millivolts range. The experiments showed that to adapt a magneto hydrodynamic channel into a system that first converted waste metabolic heat into a means to propel a magneto hydrodynamic fluid and then converted the effect caused by the fluid through the channel into electricity, would not be a viable solution.

Chapter 5: Flow Induced Vibrational Energy Recovery (FIVER) Plant

The energy conversion capabilities of flow induced vibrations have been largely overlooked. Phenomenon such as vorticy shedding and hydrodynamic wave guiding is responsible for catastrophic failures in cross flow heat exchangers, power lines and offshore oil rigs[1]. Such power exists to cause failure of steel members, and this same power could be harnessed to produce electricity in MEMS devices.

Hydrodynamic waveguides and vortex shedding are separate phenomenon and each lends innovative energy conversion theory. Here we will only examine elastic instability incurred by wave guiding since this yields the greatest amplitudes of vibration. When the flow field shifts, the force acting on immersed members will also change; these forces induce vibration amplitude instability if the energy input from the fluid exceeds the amount lost to damping in the structure.[2]

This concept is illustrated in figure 5.1. A fluid flows through an array of cylinders with a particular local velocity. The cylinders may remain stationary or oscillate slightly due to vorticy shedding at the natural frequency of the structure. However, when this local velocity matches a critical velocity distinct to the system, the array is excited into an unstable oscillation regime.

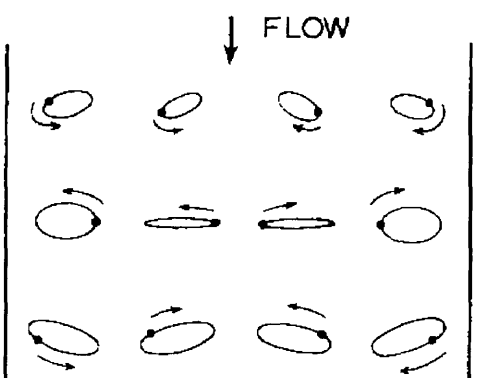

Figure 5.1. Orbits of Tube Vibration at Critical Velocity (Blevins, p. 155)

The amplitudes of vibration for two different flow experiments are included in figure 5.2. The amplitude is theoretically unbounded and indeed has been found to only be limited by the collisions between members. These impacts are responsible for the mechanical failure of cross flow heat exchanges.

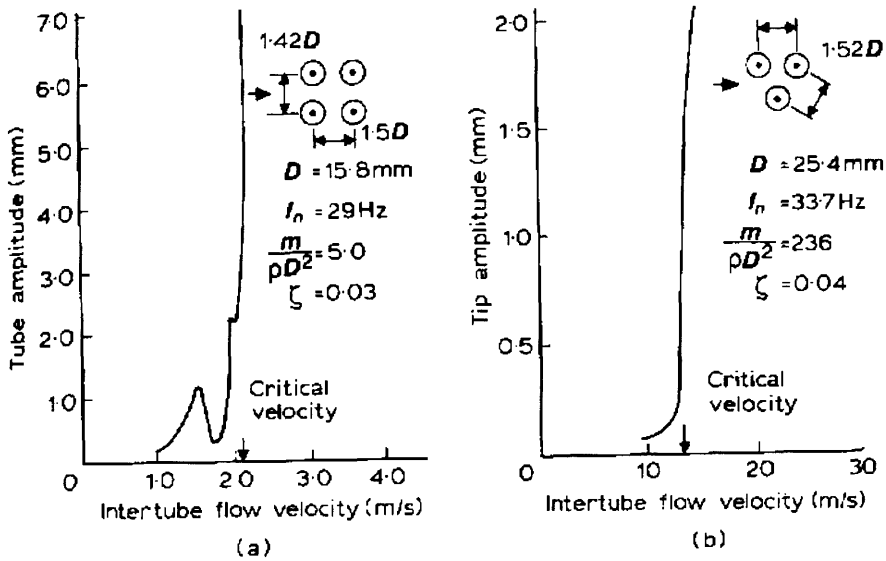

Figure 5.2. Response of arrays of tubes to cross flow. (a) Brass tubes in water flow. (b) Plastic tubes in air flow. The initial hump in 1a is attributed to vortex shedding at the natural frequency of the structure (Blevins, p. 156).

The critical velocity for the onset of instability seems to be independent of Reynolds number or turbulence factor.[3] Based on existing data, only the damping, mass and resonant frequency of the elastic members contributes to the critical velocity. Equation 5.1 is the empirical correlation for these quantities in cylindrical members and Figure 5.3 is the data set from which this correlation is derived.

$$\frac{U_{crit}}{f_n D} = C\left[\frac{m(2\pi\zeta)}{\rho D^2}\right]^a \qquad \text{(Eq. 5.1)}$$

The constants C and *a* are empirically derived, but have been found to vary slightly with mass damping. The mass damping is the ratio on the right hand side of equation 5.1, where m is the mass, zeta is the tube damping factor, rho the density of the fluid and D the outer diameter. The left hand side of equation 5.1 contains the critical velocity, cylinder diameter and resonant frequency.[4]

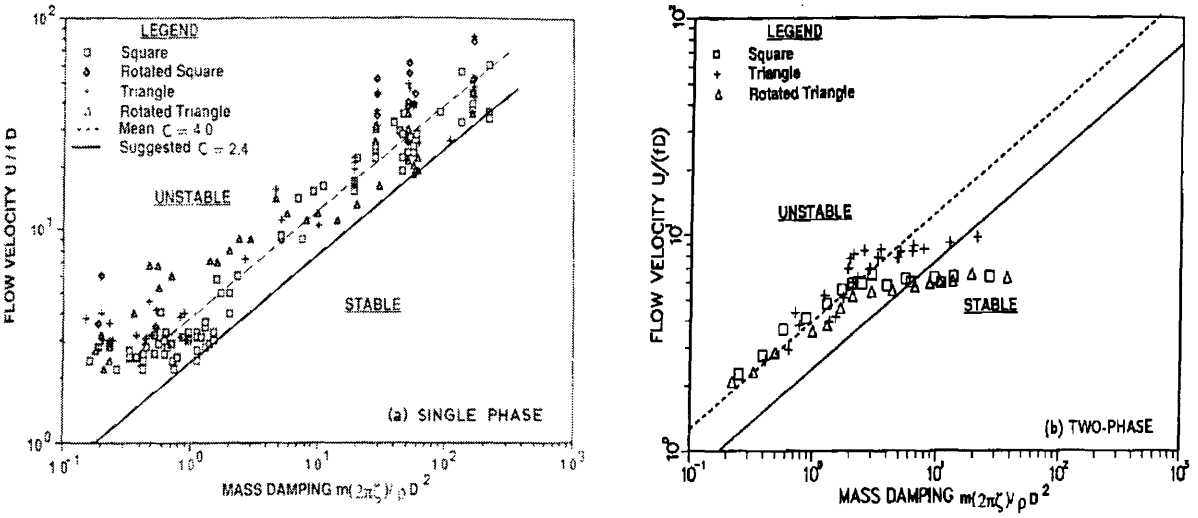

(a) (b)

Figure 5.3. Onset of instability as a function of mass damping parameter: (a) in single phase fluids, (b) in two phase mixtures. The left hand corner legend indicates what array geometry was used. The plotted lines are for a particular C value (Blevins, p. 159).

The applicable density for two phase mixtures is calculated from the void fraction, epsilon, of the flow, where the density follows from equation 5.3.

$$\varepsilon = \frac{\dot{V}_g}{\dot{V}_g + \dot{V}_l} \qquad \text{(Eq. 5.2)}$$

$$\rho = \rho_l(1-\varepsilon) + \rho_g \varepsilon \qquad \text{(Eq. 5.3)}$$

Analysis of the instability requires an accurate theoretical account of the forces acting on the vibration tube. Unfortunately, this problem has not been resolved and to date theoretical models provide only rough estimates when data is unavailable.[5] Fortunately, experiments show that the pressure drop across the array can be modeled as flow over a cylinder with an empirically based correction to the drag coefficient. The denominator in the left hand side ratio of equation 5.4 is the drag coefficient for pure flow over a cylinder; A_y is the amplitude of vibration.

$$\frac{C_D\left|A_{y>0}\right.}{C_D\left|A_{y=0}\right.} = 1 + 2.1\left(\frac{A_y}{D}\right) \qquad \text{(Eq. 5.4)}$$

If this elastic instability occurs within an array of piezo-electric elastic members, cylinder vibrations could generate electricity. A similar device has already been designed by Kim et al. for scavenging random structural vibrations. His particular design employs an inter-digitated electrode to harness the g_{33} strain mode. This particular mode utilizes the compression of the piezo material to produce power at over 30 times greater than his competitors that employ g_{31} shear strain. Likewise, the fabrication only requires three masks.[6]

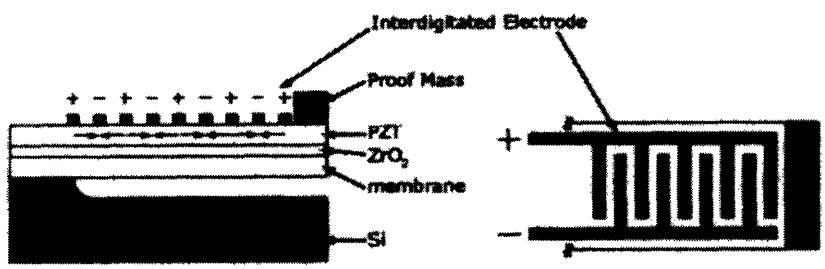

Figure 5.4. Schematic of Kim's device utilizing the d_{33} compression/tension mode. The final device is heat strained into an orientation normal to the silicon wafer. Kim et al.

Kim's device shown in figure 5.4 boasts a power density of 20 kW/m^3. Overall, the device is 170 microns tall, 220 microns wide and 1 micron thick. Structurally, it has a damping coefficient of 0.0107, first resonance at 14 kHz and a mass of 0.3 micro-grams. The charge generated per cycle was proportional to tip displacement at 4.14 x 10^{-6} C/m amplitude.[7]

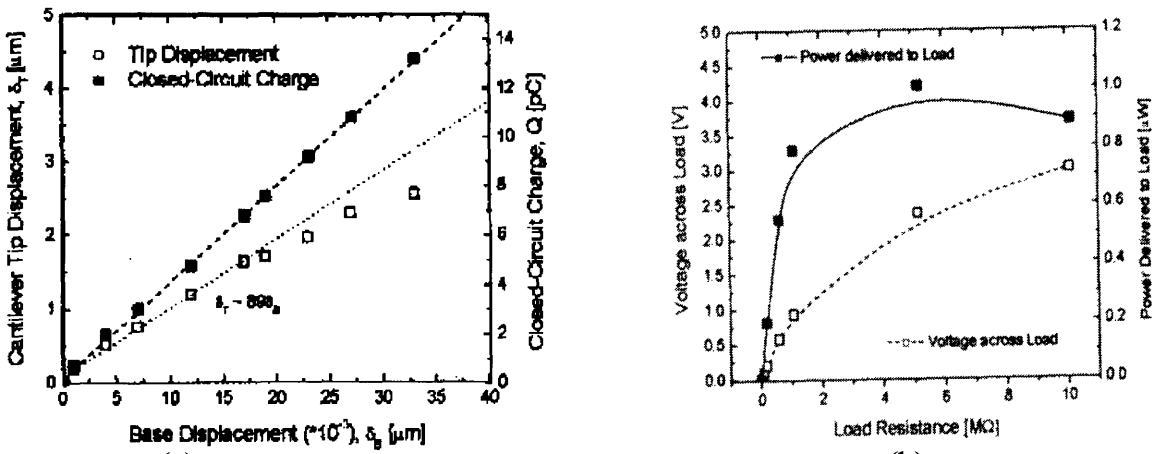

Figure 5.5. Power production parameters for MEMS device. (a) results of base shaking experiments at 14 kHz. (b) Power delivered to load at resonant frequency. Kim et al

A very effective power plant would result from the construction of a wave guide array consisting of numerous vibration energy scavengers like the above device. The power density of the device in Figure 5.4 is already comparable to chemical batteries. Likewise, the power output is at 2.4 VDC, which is a favorable condition for any signal processing equipment. For simplicity of analysis, we will assume that a 7 by 10 square array of 100 micron diameter cylinders can be fabricated with the same properties as Kim's device. The center-center spacing will be 150 microns, and the height 1200 microns. These geometric constraints are required in order to use the empirical data mentioned above.

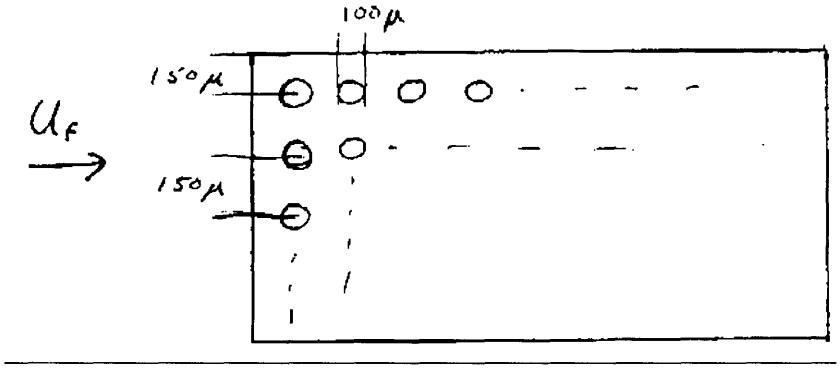

Figure 5.6. Top view of cylindrical member plant. Each member is 1200 micron tall

The square arrangement of the cylinders will influence the relationship between local velocity and free stream velocity, as well as the value of C in equation 5.1. In this geometry the free stream velocity is two thirds of the local velocity[8]. Equation 5.1 calculates the local value of the critical velocity. The local Reynold's number should be greater than 150 to ensure that vortex interactions occur.

$$\mathrm{Re} = \frac{\rho U_{crit} D}{\mu} \qquad \text{(Eq. 5.5)}$$

For this analysis, we will also assume that the fluid is a two phase mixture. This condition accommodates for applications with combustion or a condensable working fluid. In particular, we will assume a 94% void fraction and consequently an average fluid density of 41 Kg/m^3. This is a reasonable estimate for lean burning Diesel fuel or closed cycle plant operation with a condensable gas.[9] Based on the theoretical diameter, and Kim's device mass, fluid density, and damping coefficient, equation 5.1 yields 4.6 x 10^{-3} for mass damping. For this mass damping and geometry, Blevins suggests setting C = 3.9, and a = 0.21 in equation 5.1. The critical local velocity is therefore 0.68 m/s. Assuming that a slightly greater velocity will be needed to accommodate other losses, we will continue the analysis assuming a critical velocity of 0.8 m/s and 0.53 m/s free stream velocity. The resulting local Reynolds number is 170.

The actual amplitude of vibration can not be determined without experimentation. Since the dynamics of this system include an electrical energy storage mode, the response of the array can not be predicted by simple elastic theory. The amplitudes of elastic members increase indefinitely because structural damping can not compensate the energy input to the structure. This should not be the case in the piezo device since the electrical storage mode should accommodate the influx of energy.

Perhaps the local resonant activity will still induce large amplitudes, but the effects of electricity production must be explored experimentally. On the other hand, the electrical activity is proportional to velocity and hence the added damping effects will likely raise the critical velocity. By sweeping the flow speed about the critical velocity, a suitable tip displacement should be found. In any case, estimates done with the above critical velocity should still illustrate the order of magnitude for power production capabilities of this device. In that same vein, the limit on vibration amplitude is also best set by the maximum allowable strains at the base of the device.

For ceramics, the typical design failure strain limit is 10^{-3}. Elastic theory gives an order of magnitude estimate for the tip amplitude that satisfies this requirement. Within a 30% margin of error, a tip amplitude of 6.2 microns is acceptable.[10] The available two phase mixture data for elastic cylinders indicates that this displacement, and higher, often occur in similar pure elastic systems. Experimentation with a piezo array is necessary to truly determine the response of the system however the calculated tip amplitude is very plausible.[11] Furthermore, ceramic materials do not generally suffer from cyclic fatigue and the base strains can be significantly reduced by elongation of the cylinders.

The resulting electrical power is the product of charge generation rate and output voltage. The charge generation rate is a product of oscillation frequency, tip displacement (in meters) and charge generation per displacement (lambda, C/m).

$$P_e = f_n \lambda V \delta \quad \text{(Eq. 5.6)}$$

In this case, the device oscillates at its resonant frequency. With Kim's properties and the expected tip displacement, the power per cylinder is 0.9 micro-Watts, at 2.5 VDC. The volume of an entire array unit is 2.38 x 10^{-9} m^3, and contains 70 cylinders. The resulting power density of a complete single unit is therefore 26.5 kW/m^3. A single array unit occupies 2.4 mm^3 and produces 63 micro-Watts.

The pressure drop down the array depends on the drag force exerted by the cylinder.

$$F_D = \frac{1}{2} \rho U_{crit}^2 D C_D \quad \text{(Eq. 5.7)}$$

The drag coefficient is calculated from equation 5.4, where the static drag coefficient is 1.32.[12] The corrected drag coefficient is 1.49, and the resulting drag force on the cylinder is 2 x 10^{-3} N per unit length. The pressure drop across a row of cylinders is equal to the ratio of drag force to transverse tube spacing. In this case, the pressure drop across a row is 13 Pa, or 96 Pa across the entire array. The free stream velocity and the transverse cross sectional area can be used to determine the net volumetric flow rate of the mixture. Combined with the pressure drop across the array, we can calculate the power dissipated through drag.

$$P_d = \Delta P U_f A_t \quad \text{(Eq. 5.8)}$$

Furthermore, neglecting damping dissipation within the structures, we can use the calculated electric and dissipation power to determine the mechanical efficiency of conversion.

$$\eta = \frac{P_e}{P_e + P_d} \qquad \text{(Eq. 5.9)}$$

The drag dissipation for the array is 95 micro-Watts, and hence the efficiency of conversion would be 40%.

The purpose of this analysis is to show that a great potential exists within flow induced vibrations. Only the construction of this array can truly validate the utility of this conversion method. Fortunately, the calculations so far imply that there may be a simple and efficient conversion process that utilizes an otherwise injurious instability phenomenon.

The cylindrical geometry above may be harder to fabricate than a flat rectangular shape. An easier experiment may be performed with rectangular members. In fact, the army research laboratories at Adelphi, Maryland, have already produced a suitable rectangular piezo-electric cantilever array, albeit without the clever design from Kim's device.

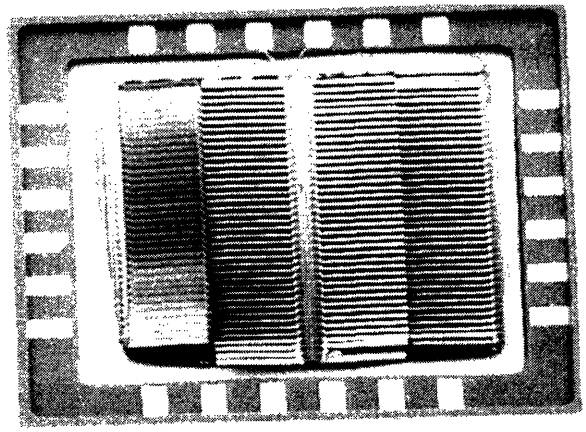

Figure 5.7. Piezoelectric vibrational energy scavenger from ARL Adelphi Labs. Members are 2 mm long (horizontal).

Provided that each member has a square cross section, the empirical data for cylindrical geometries should still be valid for order of magnitude estimates on square device properties. Assuming a 24 member array with rectangular cross sections that are 75 by 60 microns, and members 6 mm long, the final power density is 98 kW/m^3 at 40% mechanical efficiency. Alternatively, the power density is 39.2 W/kg. The details of this calculation are in Appendix D. The precise power density and efficiency can not be found without experimentation; however even at 1 order of magnitude error the remaining power density combined with the simplicity of the device is very appealing. The critical velocity is still nearly 1m/s, and the fabrication requires no more than 3 masks and a wafer bond. In fact, the ARL device needs only a few alterations before it can be tested as a flow induced vibrational energy recovery (FIVER) plant.

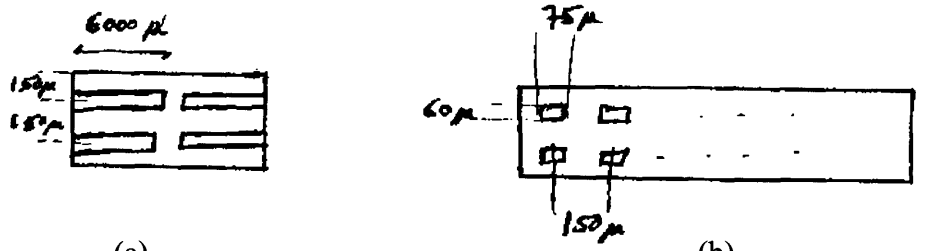

(a) (b)

Figure 5.8. Top (a) and side (b) views of square array. 6 rows of 4 cantilevers.

The desired device is essentially two individual arrays similar to that shown in figure 5.6, yet bonded to one another, face to face. At this point, experimental verification would be very simple; the specified geometries have already been created for other devices, the piezo-electric design has already been tested and validated, and the empirical fluid data exists for operation at the dimensionless scale of the desired array.

Furthermore, the simple design above could be expanded to any number of members. With back and front end silicon processing, each array could also have multiple layers and rows.

Experimentation with cantilever stiffness, flow speed, fluid density and electrical load will ultimately yield a simple device with an enormous power density and excellent efficiency. Such a power plant could easily be used with a heat pipe system for waste body heat conversion. Implementation would be simple; the plant is just installed as part of the pipe during heat pipe fabrication. On the other hand, careful attention must be paid here to convective heat transfer effects on the fluid quality down the array. Condensation on the vibrating members will certainly affect oscillation dynamics. Negative effects can be reduced, however, if the array is tuned to changes in quality and incumbent condensation; gradients in member mass or elasticity can be designed to counteract the added mass and damping effects of condensed vapor.

This device could also be used in conjunction with an octane fuel combustor. A piezo-electric micro-pump could supply a very lean fuel mixture at nearly atmospheric pressure but near the critical velocity of the plant. Normal spark ignition combustion is then used to raise the pressure of the mixture to whatever level is necessary to operate the plant. Since the pressure drop in the plant is dictated by the number of rows in the array, the combustion design can be tailored to the size of the plant. On the other hand, proper use of nozzles can manipulate a higher gas pressure into the proper range of pressure and velocity. The limiting factor here is maximum allowable load on the cantilever system. Again requiring base strains to be less than $5x10^{-4}$, the maximum allowable pressure at a

unit inlet is 1.560 kPa. With this limit on pressure drop across an array, individual plants can have as many as 340 cantilevers.

Operating at a lower temperature may alleviate the waste heat and dangerous thermal signature of the generator. Even with the resulting drop in overall efficiency, the high power density of the unit sustains its viability as a mobile power plant. Ideally, no surface or exit stream of the device would be hotter than 70 degrees C. The process is essentially limited by the lowest fuel density allowed by combustion. An energy balance can be made between the enthalpy of combustion of octane and the enthalpy of the products to determine the air to fuel ratio for a desired pressure and temperature. The correct combination between mixture compression and excess atmosphere should yield a low gas temperature but adequate velocity and pressure for plant operation. Humidification of the products may also be necessary in order to raise the effective density of the two phase mixture. The final vision of this device is a power plant the size of a poker chip that runs off a thimble sized Diesel fuel reservoir.

If numerous small plants are used, each with their own combustor, then the necessary pressure and temperature rise in each combustor will always be small. Essentially, this is a parallel generator design, where it is only the electrical outputs of each plant that unify the system. The benefit of this scheme is that each combustor will only yield products moderately above room temperature. Juxtaposed with the cost of individually supplying a vast network of combustors with the proper fuel to air mixture, only experimentation can validate the concept. Hopefully this idea will offer a viable alternative to micro-turbine and fuel cell research.

[1] Blevins, Robert D, " Flow Induced Vibrations." (Van Nostrand Rheinhold, New York. 1990). p. 153
[2] ibid.
[3] ibid, p. 157
[4] ibid. p. 158
[5] ibid. p. 161
[6] Kim, Sang G. "Piezoelectric Micro Power Generation for Energy Harvesting". Mechanical Engineering Department, MIT, working paper
[7] ibid.
[8] Blevins, Robert D, " Flow Induced Vibrations." (Van Nostrand Rheinhold, New York. 1990). p. 156
[9] Pettigrew, M. J. "Vibration of Tube Bundles in Two Phase Cross-flow: Part 3 – Turbulence induced excitation" 1998 International Symposium on Flow Induced Vibration and Noise, Vol. 2, p. 112.
[10] Crandahl, S. "Introduction to Solid Mechanics" p. 125
[11] Pettigrew, M. J. "Vibration of Tube Bundles in Two Phase Cross-flow: Part 3 – Turbulence induced excitation" 1998 International Symposium on Flow Induced Vibration and Noise, Vol. 2, p. 115
[12] Blevins, Robert D, " Flow Induced Vibrations." (Van Nostrand Rheinhold, New York. 1990). p. 96

Chapter 6: Conclusions

Power limitations on the dismounted soldier pose a serious threat to his survival and the success of his mission. The soldier of today can not wait until 2015 and the expected deployment of high output mobile power plants. A simple and effective solution should reach the soldier within the next year.

In pursuit of this goal we have examined several power systems that utilize waste metabolic heat for electricity production. Simple heat engine calculations show that such a power system is formidable at ambient temperatures no greater than 15 – 17 degrees Celsius. This estimate accounts for heat transfer losses in the system, mechanical inefficiencies of the power plant and the necessary temperature differentials for heat rejection. Considering the time average daily waste heat output of a typical man, our mobile power plant should supply 3W over a 24 hour period.

The key to success for this concept is an efficient power conversion process. Heat pipes offer the simplest and most direct route for harvesting waste heat. Their potential for discrete integration into existing soldier garments makes heat pipes especially attractive. The resulting vapor is suitable for a variety of mechanical conversion devices. The most promising of such novel power converters is the flow induced vibrational energy recovery (FIVER) plant. Based on empirical data and proven existing technologies, this power plant boasts a 98 kW/m^3 (39.2 W/kg) power density at a mechanical efficiency of 40%. Simple experiments were also deduced to improve the properties of this device, and a course of research was proposed to extend this plant into an octane combustion based operation.

MHD conversion devices were also explored in this study. While theory predicts excellent efficiency and high power density, such generators are limited in their means of coupling to a Rankine system. Despite its operation advantages at the small scale, an effective gas – liquid metal pump does not yet exist to make MHD generators a reality. Our experimental data corroborates with this conclusion.

Similarly, modern thermoelectric technology does not position thermoelectrics as an effective method for waste body heat conversion. This is primarily a result of the extremely narrow range for thermoelectric operation. The successful application of thermoelectrics requires much greater temperature gradients than those seen in waste metabolic heat transfer.

Not only does waste body heat recovery offer a simple and quick solution to the soldier energy crisis, but it also has innate microclimate control abilities. By harvesting waste heat, this system also prevents thermal energy storage in the soldiers' garments. This effective cooling has been proven to enhance the endurance of the soldier during strenuous activities.

It is our sincere hope that this simple alternative energy program may blossom into an effective mobile power solution. The acceptable conversion efficiency and multi-faceted effects of mobile power production via waste body heat recovery make this system an ideal solution to the soldier energy crisis.

APPENDIX A

See Figure 4.1 for schematic of theoretical device

Assumptions:

1. External magnetic field is source-free/uniform/time-invariant:
   $B_0 = \mu_0 H$
   $\vec{B} = \left(b(y,z),\ B_0,\ 0\right)$
2. Flow is well-developed/time-invariant:
   $\vec{v} = \left(u(y,z),\ 0,\ 0\right)$
3. Constant pressure gradient along x-axis:
   $\Delta_p \triangleq p_{out} - p_{in}$
   $\partial p / \partial x = \frac{\Delta_p}{L} = (const.)$
4. No volumetric body forces $(\vec{f})$ of non-EM origin (i.e. gravity)
5. Perfectly conducting electrodes:
   $\sigma_{electrode} = \infty$
6. Perfectly insulating non-conductive walls:
   $\sigma_{insulating\ wall} = 0$

Basic Equations:

1. $\vec{\nabla} \cdot \vec{B} = 0$
2. $\vec{\nabla} \cdot \vec{J} = 0$ $\quad (\vec{J} \triangleq \text{current density})$
3. $\vec{\nabla} \times \vec{E} = 0$
4. $\vec{\nabla} \times \vec{B} = \mu_0 \vec{J}$ $\quad$ (Ampere's Law)
5. $\vec{J} = \sigma(\vec{E} + \vec{v} \times \vec{B})$ $\quad$ (Ohm's Law)
6. $\vec{F_L} = \vec{J} \times \vec{B}$ $\quad (\vec{F_L} \triangleq \text{Lorenz force})$
7. $\rho\left[\frac{\partial}{\partial t}\vec{v} + (\vec{v} \cdot \vec{\nabla})\vec{v}\right] = -\nabla p + \rho\upsilon\nabla^2\vec{v} + \vec{f} + \vec{F_L}$ $\quad$ (Momentum equation)

$$\boxed{\frac{\partial^2 u}{\partial y^2} + \frac{\partial^2 u}{\partial z^2} + \frac{B_0}{\mu_0 \rho \upsilon}\frac{\partial b}{\partial y} = \frac{\Delta_p}{\rho \upsilon L} \quad \text{and} \quad \frac{\partial^2 b}{\partial y^2} + \frac{\partial^2 b}{\partial z^2} + \sigma\mu_0 B_0 \frac{\partial u}{\partial y} = 0}$$

Boundary Conditions:

Let $\Gamma_y \triangleq \{(y, \pm d)\}_{y=-a}^{a}$ and $\Gamma_z \triangleq \{(\pm a, z)\}_{z=-d}^{d}$ represent the electrode and insulating walls (resp.), then

$u|_{\Gamma_y \cup \Gamma_z} = 0$ $\quad$ (no-slip condition)

$\left.\frac{\partial b}{\partial z}\right|_{\Gamma_y} = 0$ $\quad \left(\text{since } E_y|_{\Gamma_y} = 0\right)$

$\left.\frac{\partial b}{\partial z}\right|_{\Gamma_z} = 0$ $\quad \left(\text{since } J_y|_{\Gamma_y} = 0\right)$

$I \text{ (electrical current)} \triangleq \int_0^L \int_{-a}^{a} J_z\, dy dx \ \Rightarrow\ b|_{y=\pm a} = \frac{\mp I \mu_0}{2L}$

Equation for terminal voltage drop as a function of flow rate and current:

$$V_t = -\frac{dI}{a\sigma L} + \frac{B_0 Q}{2a} \quad \text{where } Q \triangleq \int_{-d}^{d}\int_{-a}^{a} u(y,z)\,dydz \text{ is the volumetric flow rate}$$

Equations for open-circuit voltage and short-circuit current:

$$V_{t_{oc}} = \frac{B_0 Q_{oc}}{2a} \qquad \text{where } Q_{oc} \text{ is the open-circuit flow rate}$$

$$I_{sc} = \frac{LB_0\sigma Q_{sc}}{2d} \qquad \text{where } Q_{sc} \text{ is the short-circuit flow rate}$$

Power calculations:

$$P(Q,I) = IV = \frac{B_0 QI}{2a} - \frac{dI^2}{a\sigma L}$$

Efficiency:

$$\eta \triangleq \frac{P}{\Delta_p Q} = \frac{B_0 I}{\Delta_p \cdot 2a} - \frac{dI^2}{\Delta_p Q a\sigma L}$$

Internal resistance of the channel:

$$R_i = \frac{d}{a\sigma L}$$

Optimal Operating Point

At the point where the efficiency is maximized:

$$I^* = \frac{V_{t_{oc}} - \sqrt{R_i \cdot I_{sc} \cdot V_{t_{oc}}}}{\left(\frac{V_{t_{oc}}}{I_{sc}} - R_i\right)}$$

$$V_t^* = \left(\frac{V_{t_{oc}}}{I_{sc}}\right) \cdot \frac{\sqrt{R_i \cdot I_{sc} \cdot V_{t_{oc}}} - R_i \cdot I_{sc}}{\left(\frac{V_{t_{oc}}}{I_{sc}} - R_i\right)}$$

$$P^* = \left(\frac{V_{t_{oc}}}{I_{sc}}\right) \cdot \frac{\left(V_{t_{oc}} - \sqrt{R_i \cdot I_{sc} \cdot V_{t_{oc}}}\right)\left(\sqrt{R_i \cdot I_{sc} \cdot V_{t_{oc}}} - R_i \cdot I_{sc}\right)}{\left(\frac{V_{t_{oc}}}{I_{sc}} - R_i\right)^2}$$

$$\eta^* = \left(\frac{B_0}{-\Delta_p \cdot 2a}\right) \cdot \left(\frac{V_{t_{oc}}}{I_{sc}}\right) \cdot \left(\frac{\sqrt{V_{t_{oc}}} - \sqrt{R_i \cdot I_{sc}}}{\frac{V_{t_{oc}}}{I_{sc}} - R_i}\right)^2$$

Magnetohydrodynamics References:

Müller, U. and Büler, L.: 2001, *Magnetofluiddynamics in Channels and Containers*, Springer-Verlag, Berlin, Heidelberg, New York.

Hughes, W. F. and Young, F. J.: 1966, *The Electromagnetics of Fluids*, John Wiley & Sons Inc., New York, London, Sydney.

Shercliff, J. A.: 1965, *A Textbook of Magnetohydrodynamics*, Pergamon Press, Oxford.

APPENDIX B

Images of all the magneto hydrodynamic channels are listed below.

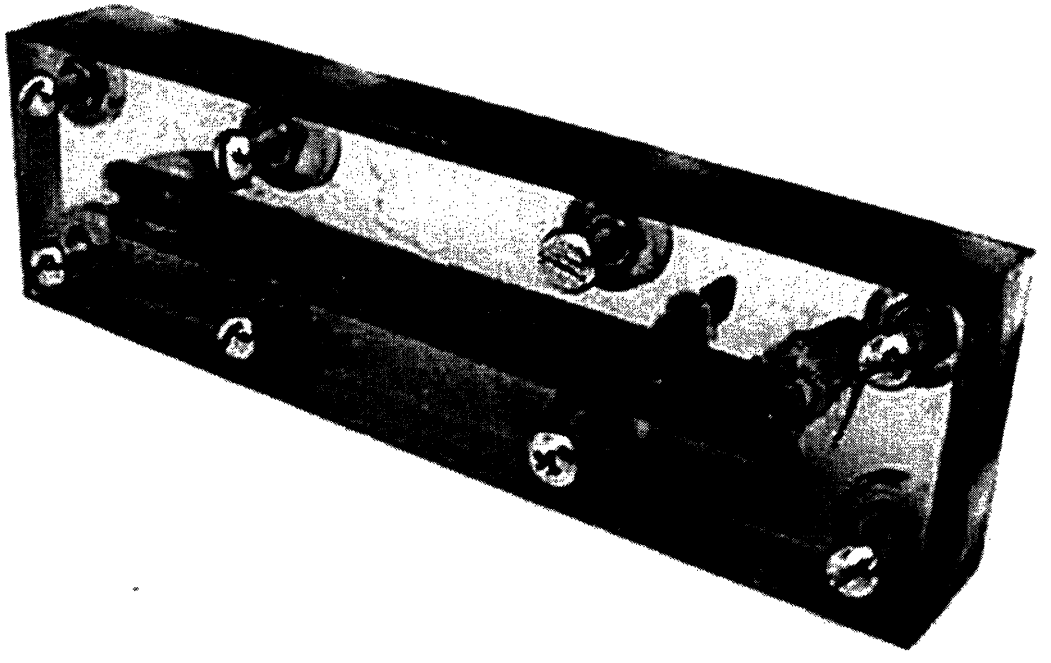

Figure B.1. Completed first generation (G1) magneto hydrodynamic channel with machine screws, tubing connectors and copper bar leads. The G1 measured 7" x 2" x 1.05".

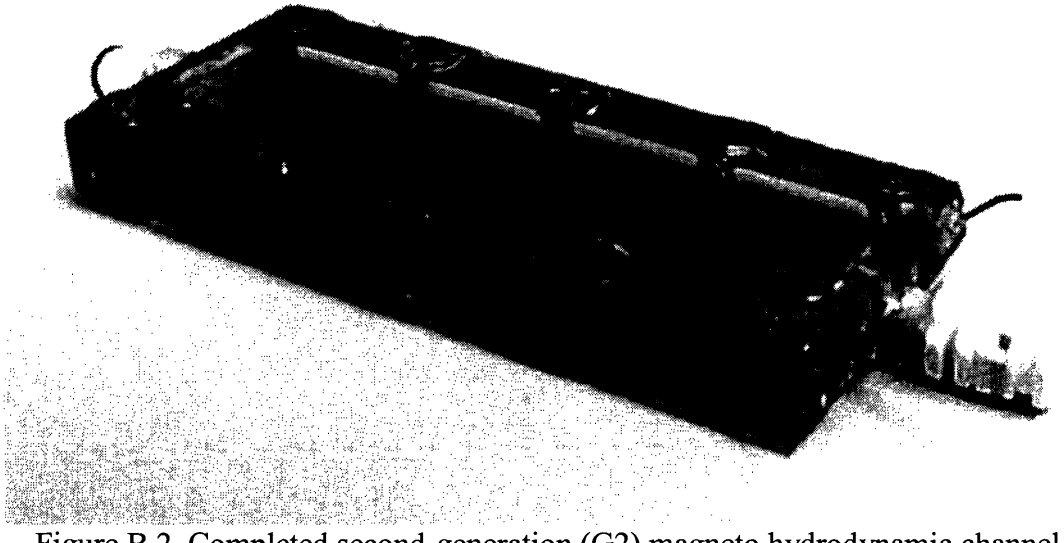

Figure B.2. Completed second-generation (G2) magneto hydrodynamic channel with machine screws, tubing connectors and wire leads. The G2 measured 4" x 2" x 0.5"

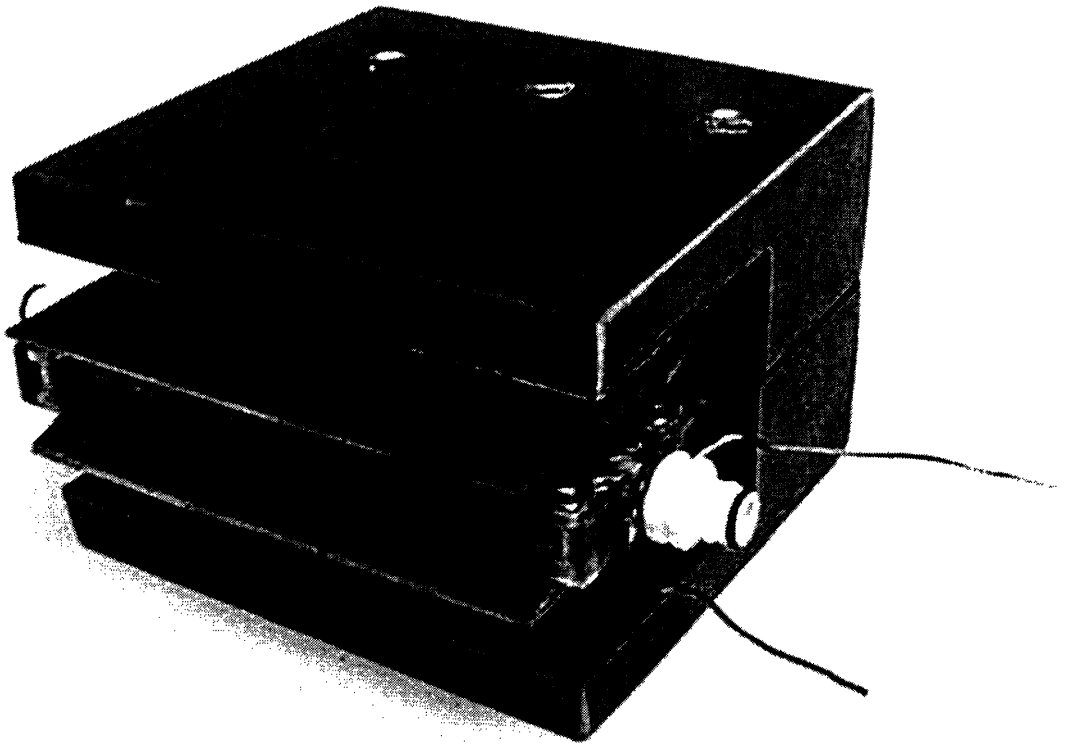

Fig. B.3. Completed third generation (G3) magneto hydrodynamic channel fully assembled with the magnetic flux focuser. The G3 measured 4" x 1.56" x 0.5". The magnetic flux focuser measured 4" x 3.25" x 2.24".

APPENDIX C

Contained herein are the necessary part drawings for the apparatuses constructed. Redundant dimensions among drawing groups are omitted. Because of image conversion into this word processor, the 1:1 scale of the drawings has not been preserved.

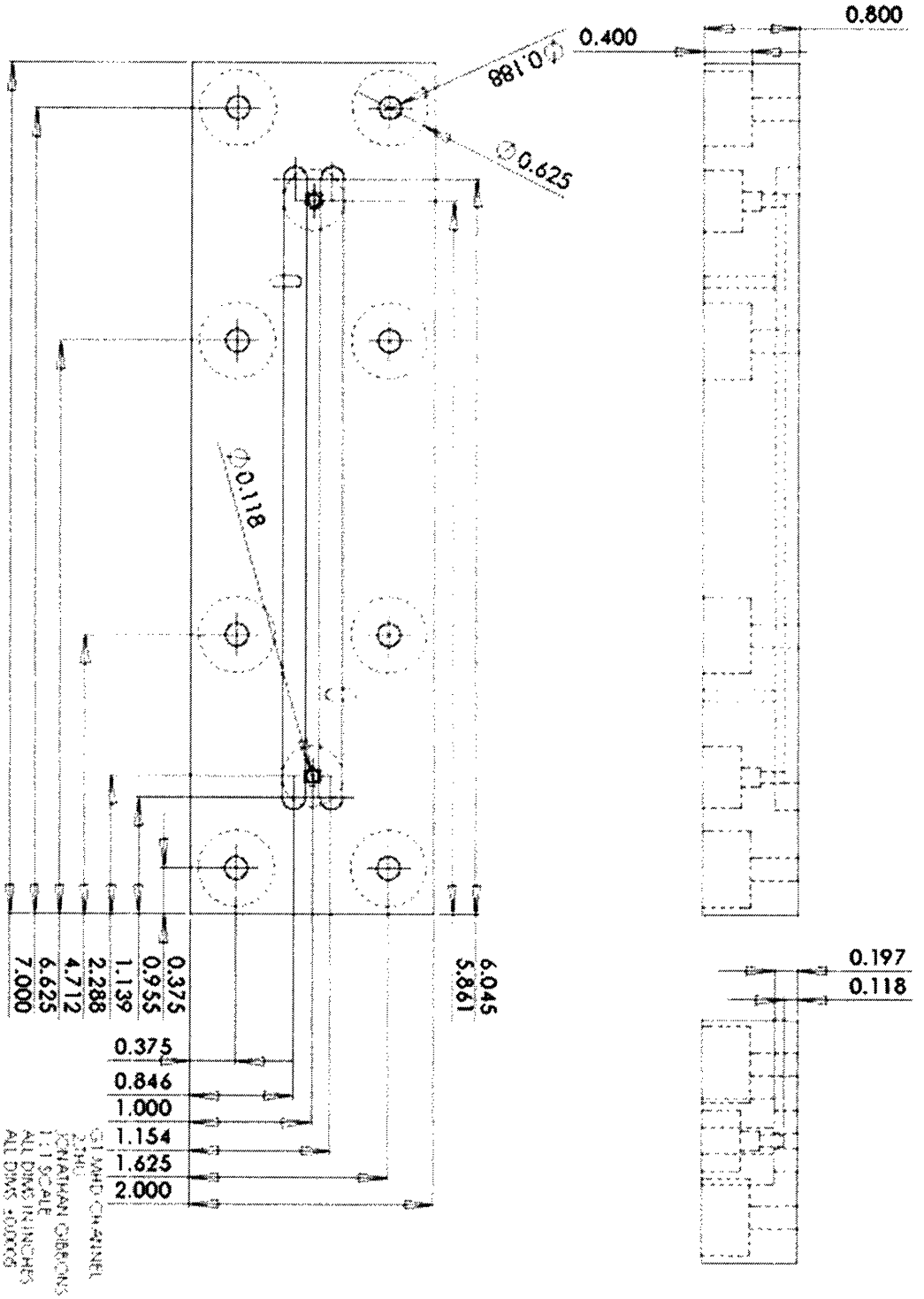

Figure C.1. G1 LEXAN Channel.

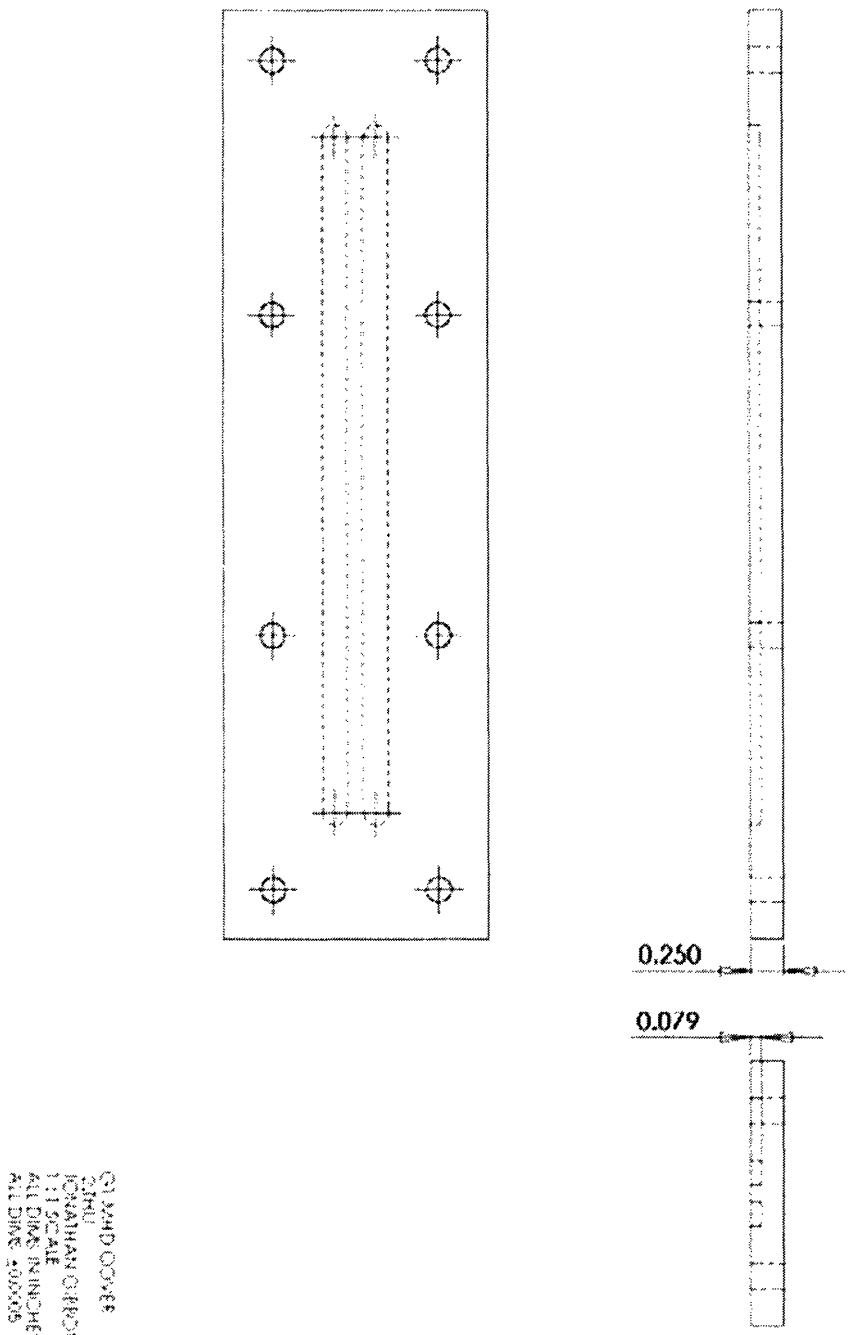

Figure C.2. G1 LEXAN Channel Cover.

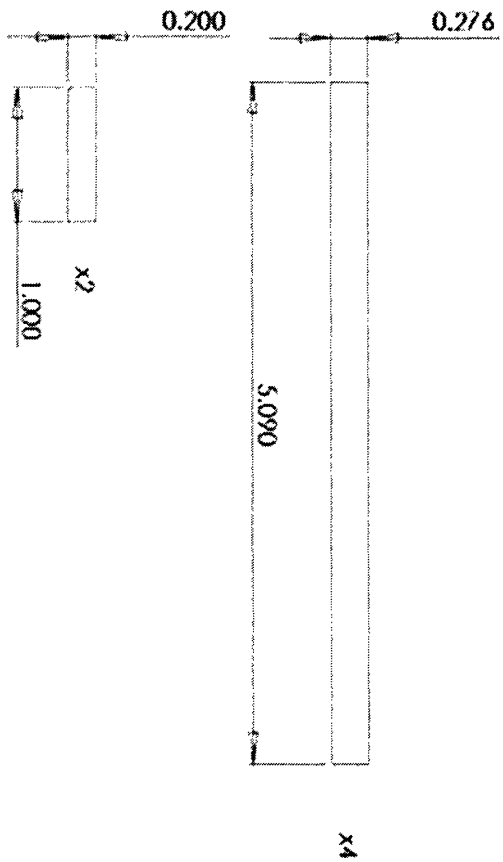

Figure C.3. G1 Copper Electrodes.

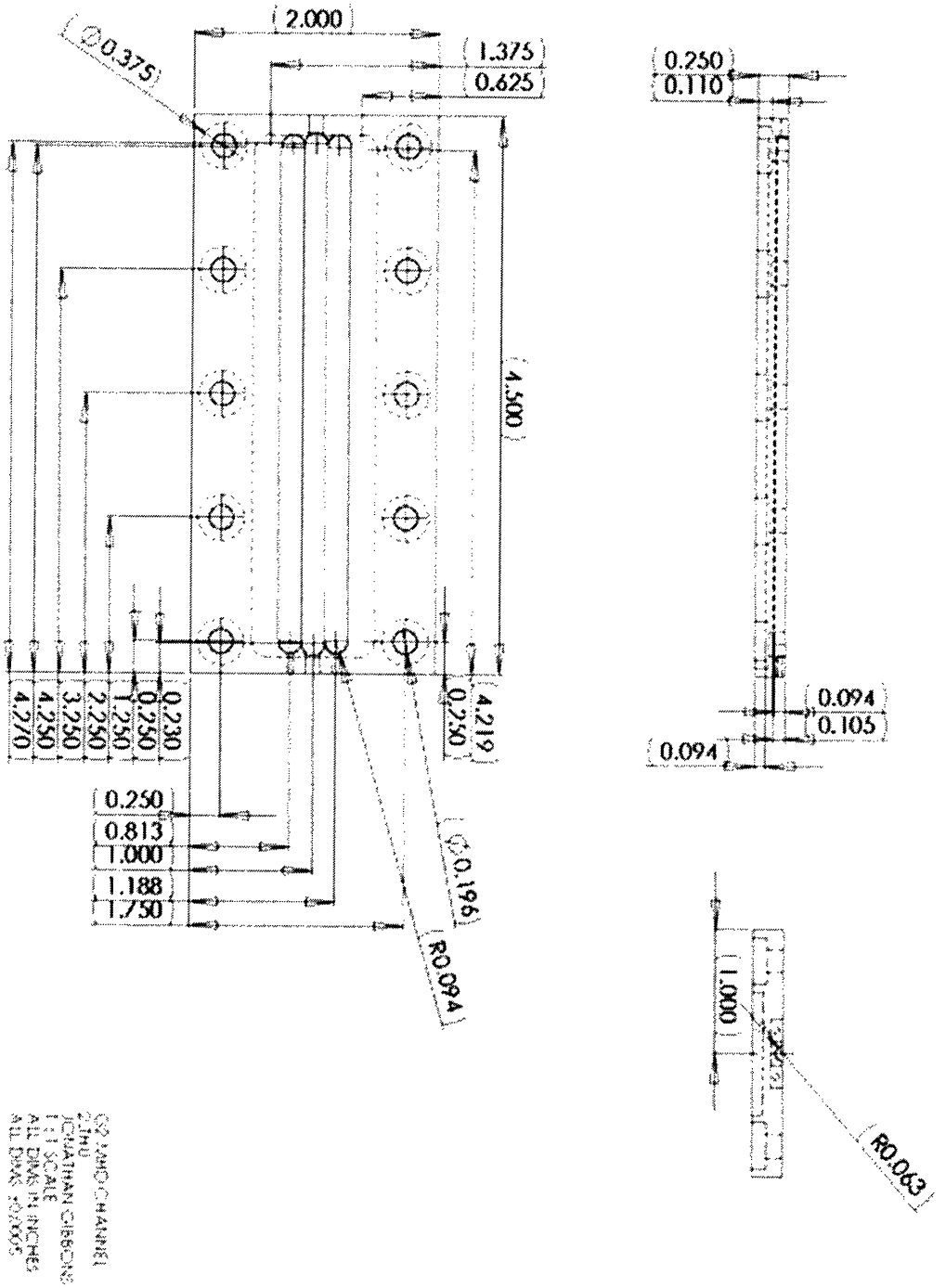

Figure C.4. G2 LEXAN Channel.

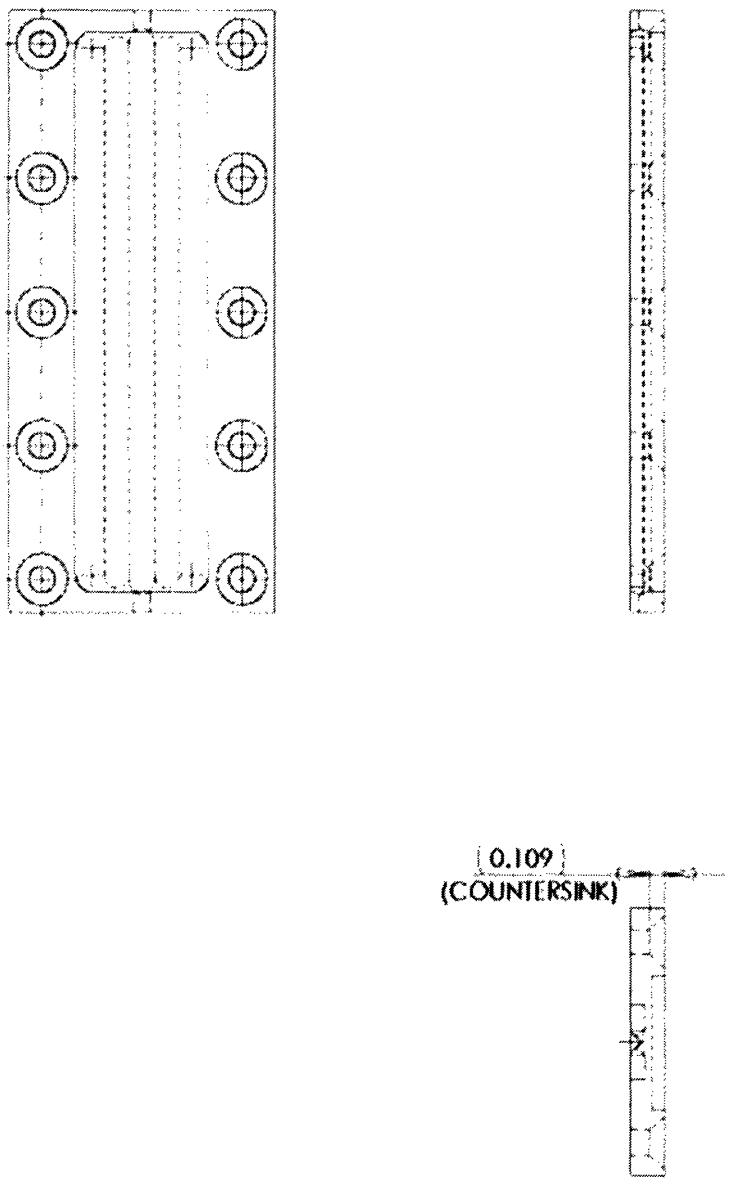

Figure C.5. G2 LEXAN Channel Cover.

Figure C.6. G2 Copper Electrodes.

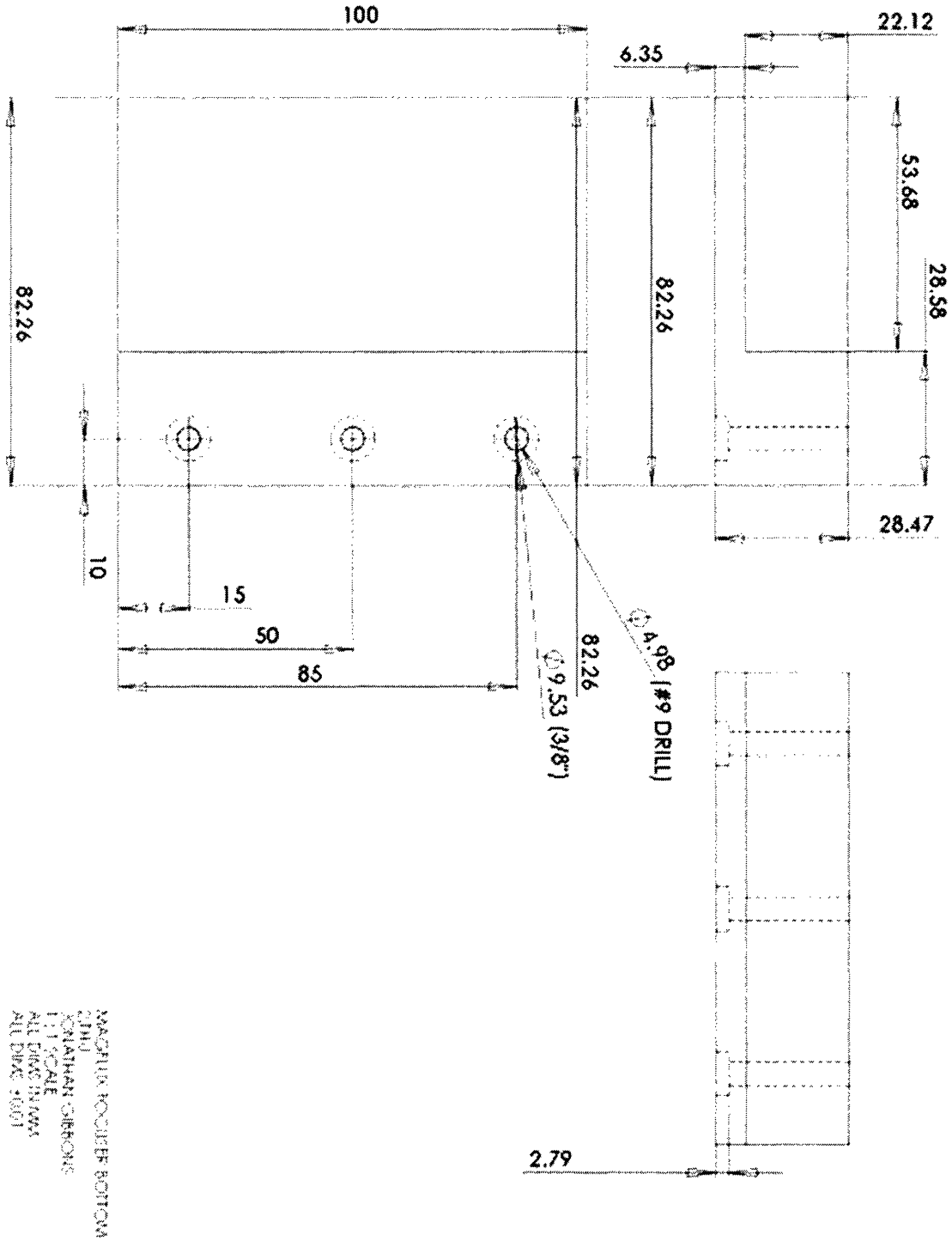

Figure C.7. M54 Steel Magnetic Flux Bottom L-Plate.

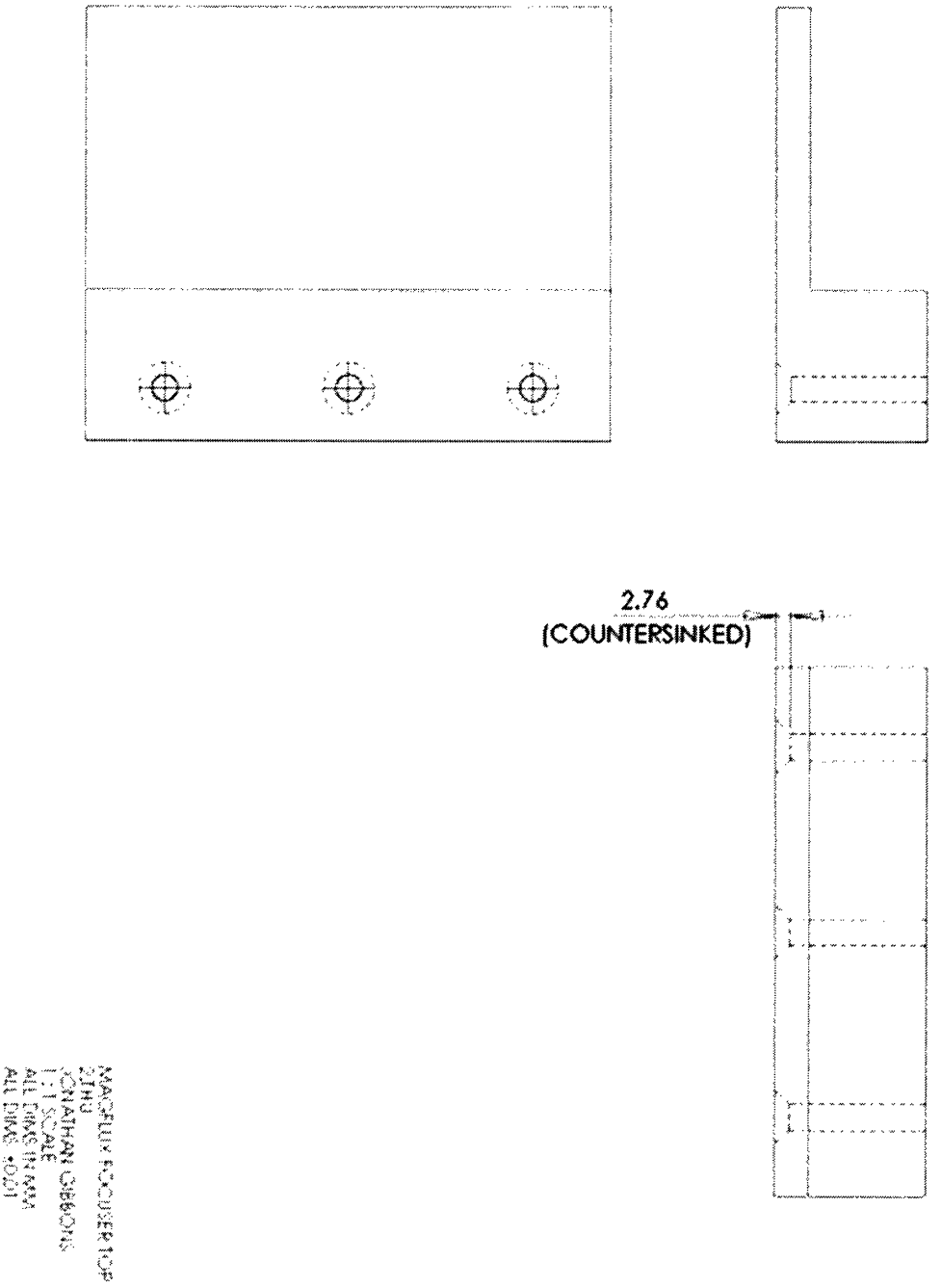

Figure C.8. M54 Steel Magnetic Flux Top L-Plate.

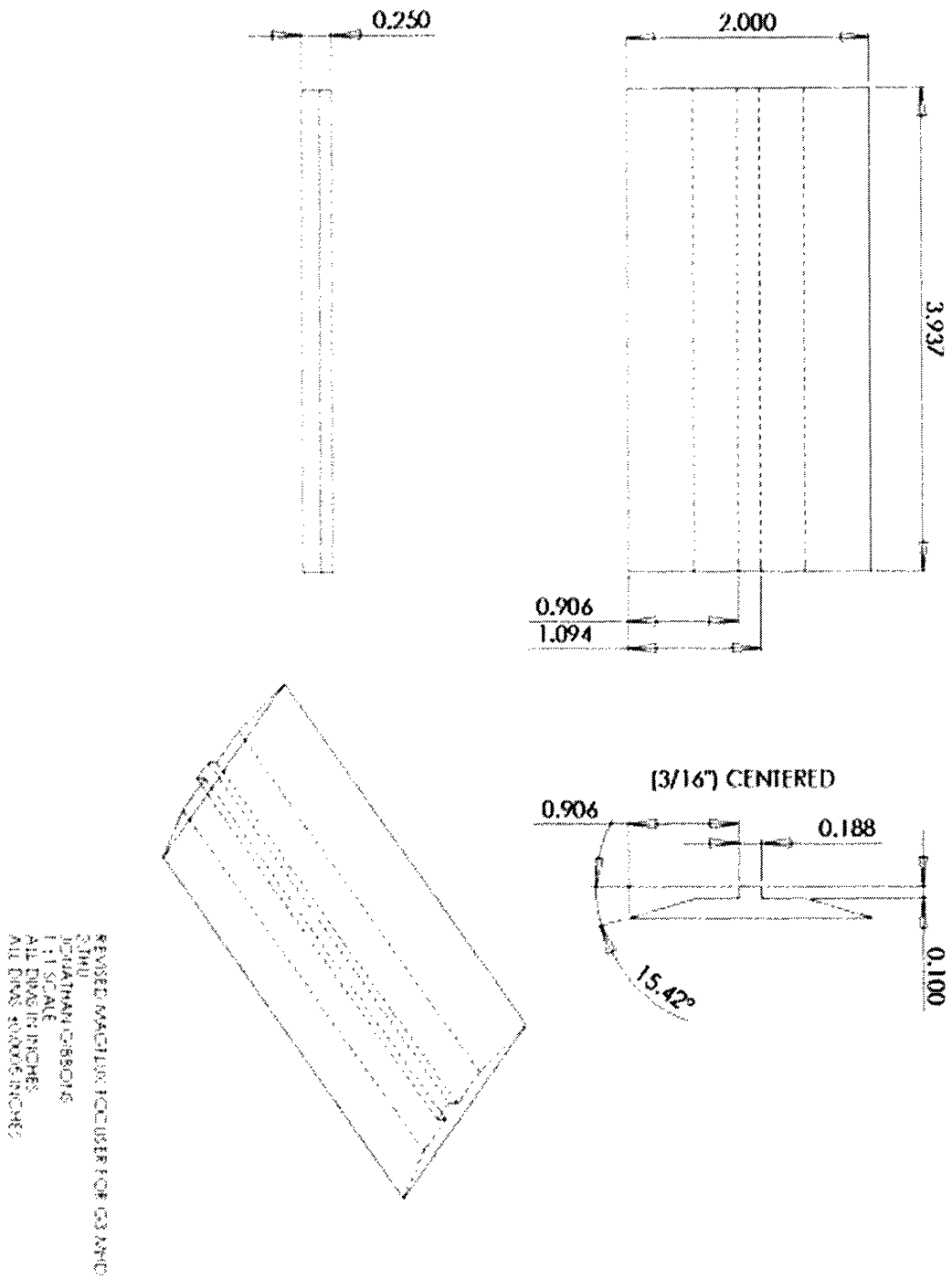

Figure C.9. M54 Steel Magnetic Flux Focuser. A set of two angled focuser parts are required to complete the magnetic circuit.

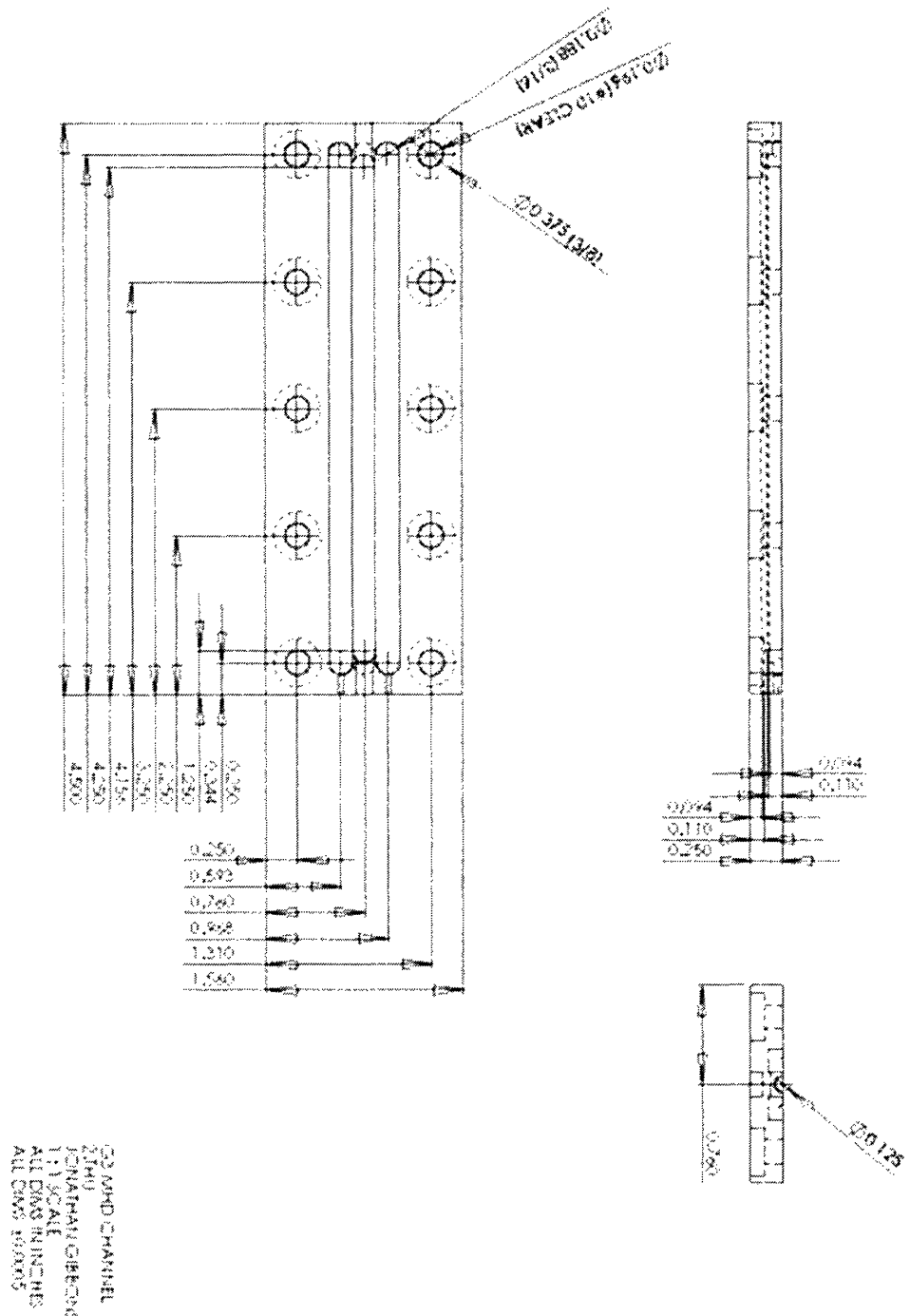

Figure C.10. G3 LEXAN Channel.

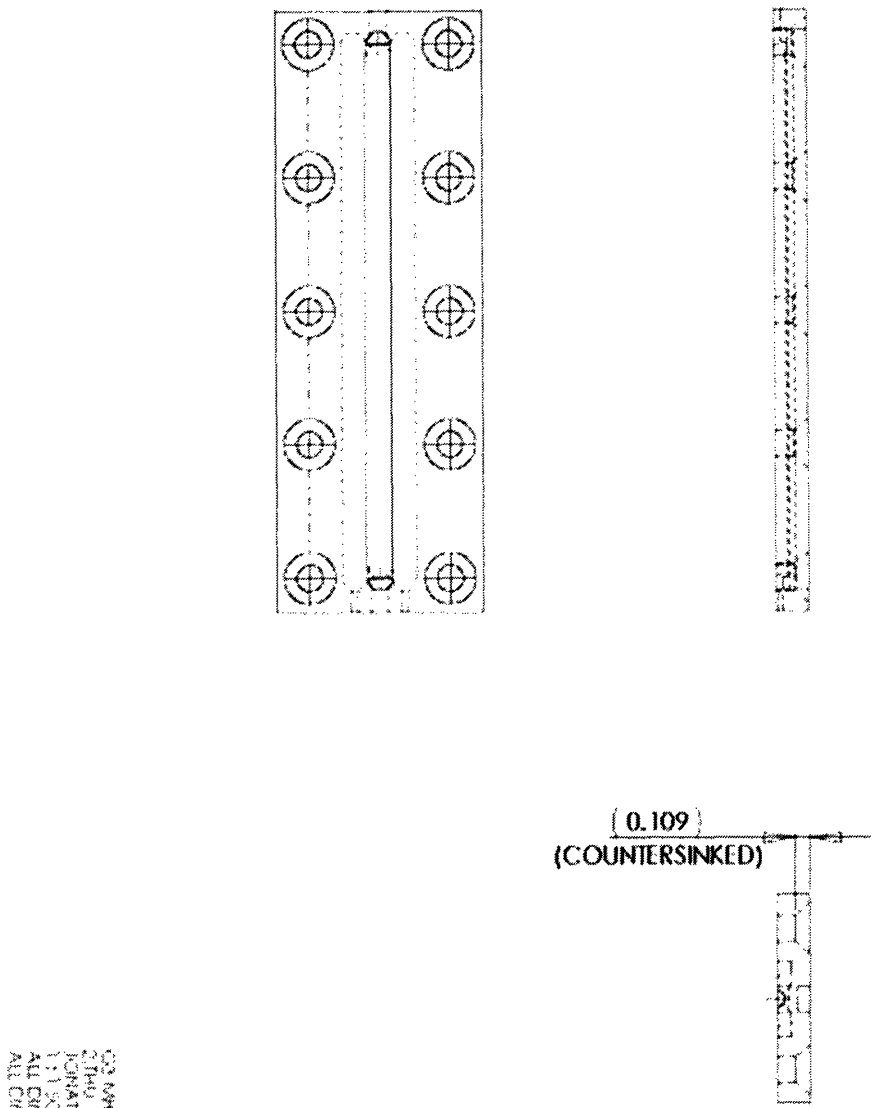

Figure C.11. G3 LEXAN Channel Cover.

Figure C.12. G3 Copper Electrodes.

APPENDIX D

Refer to figure 5.8 for diagram

$\lambda := 4.14 \cdot 10^{-6}$
Charge generated per tip displacement C/m

$\rho 1 := 500$
Zinc and Silicon Oxide Composite density kg/m^3

$E := 150 \cdot 10^{9}$
Composite modulus of Elasticity, Pa

$\rho := 21$
Fluid density 98% void fraction kg/m^3

$\mu := 1 \cdot 10^{-5}$
Fluid Viscosity Pas

$\zeta := .0106$
Structural damping Coefficient

$v := 2.5$
DC Voltage from plant V

$N := 24$
Number of members in array

$D := 75 \cdot 10^{-6}$
width of member (m)

$t := 60 \cdot 10^{-6}$
Thickness of member (m)

$n := 100$
ratio of member length to thickness

$P := 2D$
Center to center spacing for square, inline array

$L := n \cdot t$
length of member

The analysis assumes that at, or very near the critical velocity, a flow speed can acheive the maximum tip displacement which is defined as delta below. This max displacement represents a strain of 3 ten thousandths. Such a displacement has been found in many documented experiments and should exist for this system as well.
Furthermore the cylindrical theory is used here despite the square cross section. The predicted results are not expected to change very much for a near square cylinder in cross flow versus a round cyclinder. Obviously, the flow details are altered by the square cross section, however, order of magnitude estimates are still valid by the cylindrical theory, provided that the member is nearly square in cross section. Pure elastic theory is used to calculate natural frequency and tip displacement. Experimentation is necessary to determine the true physical properties of this power plant.

$m := \rho 1 \cdot (t D) L$
mass of beam

$$f := \left[\frac{\left[E \cdot t^3 \cdot (D) \right]}{4m \cdot \left(L^3 \right)} \right]^{.5}$$
resonant frequency

$$U := 3.9 f \cdot D \cdot \left[\frac{(6 \cdot \zeta \cdot m)}{\rho \cdot D^2} \right]^{.21}$$
critical velocity for power transmission

$$R := (\rho) \frac{U \cdot D}{\mu}$$
Reynolds Number

$$v := \left(\frac{2}{3} \right) \cdot U$$
Free Stream Velocity

$F := \rho \cdot v^2 \cdot D \cdot 1.7$
Drag Force per unit length

$$\Delta P := \frac{F}{P}$$

Pressure Drop
Per row

$$\delta := 2 \cdot 10^{-4} \cdot \frac{L^2}{t}$$

Max tip displacement

$$\Delta := 2 \cdot L \cdot (3 \cdot D + P)$$

Transverse Area

$$\Lambda := \Lambda \cdot (3 \cdot D + 5 \cdot P)$$

Volume of Plant

$$Q := U \cdot A$$

Flow rate

$$\sigma := Q \cdot 6 \cdot \Delta P$$

Hydrodynamic loss for 6 rows

$$\omega := N \cdot \lambda \cdot \delta \cdot f \cdot v$$

Electric Power

$$\eta := \frac{\omega}{(\omega + \sigma)}$$

Efficiency

$$\phi := \frac{\omega}{\Lambda}$$

Power Density

$f = 1.443 \times 10^{4}$ Hz $R = 236.423$ $U = 1.501 \frac{m}{s}$ $\eta = 0.373$ $\phi = 9.806 \times 10^{4} \frac{W}{m^3}$

$\delta = 1.2 \times 10^{-4}$ $L = 6 \times 10^{-3}$ $t = 6 \times 10^{-5}$